CHAPTER 3

Direct Methanol Fuel Cells

Keith Scott* and **Lei Xing**

Contents

School of Chemical Engineering and Advanced Materials, University of Newcastle, Newcastle, United Kingdom
* Corresponding author, E-mail address: k.scott@ncl.ac.uk

Advances in Chemical Engineering, Volume 41
ISSN 0065-2377, DOI: 10.1016/B978-0-12-386874-9.00005-1

Abstract Direct methanol fuel cells are suitable power sources for a range of mobile applications, due to the convenience of storage of the liquid fuel. The chapter reviews the principles of operation and models which have been developed to create viable methanol powered fuel cells. In particular models which consider the dynamic response of power and thermal behavior are reviewed to aid in development of control strategies. The DMFC responds quite rapidly to changes in operating conditions and is a suitable power source for portable applications where variations in operating conditions arise.

ABBREVIATIONS

1D	one dimensional
2D	two dimensional
3D	three dimensional
B–V	Butler–Volmer
CVA	canonical variate analysis
DHE	dynamic hydrogen electrode
DMFC	direct methanol fuel cell
e.m.f	electromotive force
EOD	electro-osmotic drag
MEA	membrane electrode assembly
MOR	methanol oxidation reaction
PEMFC	proton exchange membrane fuel cell
RTD	residence time distribution
SHE	standard hydrogen electrode
SPE	solid polymer electrolyte

1. INTRODUCTION

The direct electro-oxidation of methanol in a fuel cell has been a subject of study for more than three decades. The early cell designs utilized aqueous sulfuric acid electrolyte at about 60°C. In a fuel cell employing an acid electrolyte, methanol is directly oxidized to carbon dioxide at the anode:

$$CH_3OH + H_2O \rightarrow CO_2 \uparrow + 6H^+ + 6e^- \quad (1)$$

The thermodynamic potential (E^0) for reaction (1) calculated from the standard chemical potentials at 25°C is 0.03 V versus SHE. At the cathode, oxygen gas combines with the protons and electrons and is reduced to water:

$$\frac{3}{2}O_2 + 6H^+ + 6e^- \rightarrow 3H_2O \quad (2)$$

The thermodynamic potential (E_c^0) for reaction (2) is 1.23 V (vs. SHE). Accordingly, the net cell reaction is

$$CH_3OH + \frac{3}{2}O_2 \rightarrow 2H_2O + CO_2 \quad (3)$$

The standard electromotive force (e.m.f.), E_{aq}^0=1.20 V.

A main drawback of direct methanol fuel cells (DMFCs) is the very sluggish anode reaction, which coupled with the inefficient cathode reaction, gives rise to low overall performance, particularly at low temperatures. The potential efficiency (ε_f) of a DMFC for an operational cell e.m.f. (E) of 0.5 V is about 40% and the specific energy (W) is $-\Delta G^\circ/3600\times M = (702\times10^3)/(3600\times0.032)=6.1\,\text{kWh kg}^{-1}$.

In the 1980s, it is realized that a considerable increase in the efficiency might be obtained in which the liquid electrolyte is replaced by a thin proton-conducting polymer membrane such as Nafion®—a perfluorosulfonic acid polymer (Shukla *et al.*, 2002a), which is shown schematically in Figure 1.

In this DMFC, methanol dissolved in water is supplied to its anode but tends to pass through the membrane and affects the performance of the cathode (Gurau and Smotkin, 2002; Heinzel and Barragán, 1999; Munichandraiah *et al.*, 2003). Therefore, a fundamental limitation in the practical realization of such a DMFC is the existence of electrochemical losses at both anode and cathode arising mainly due to the electrocatalytic restrictions and methanol crossover though the membranes associated with diffusion and electro-osmotic drag (EOD).

A typical polarization curve for a DMFC shown schematically in Figure 2 illustrates the limitations to the performance of the DMFC. Although the thermodynamic potential for reaction (1) is 0.03 V (vs. SHE), because of the number of electrons involved, the equilibrium value is not readily realizable, even with the best possible electrocatalysts. Furthermore, because of the high degree of irreversibility of reaction (2), even under open-circuit conditions, the overpotential at the oxygen electrode is about 0.2 V which represents a loss of about 20% from the theoretical efficiency. With the DMFC, there is another inherent loss of approximately 0.1 V at the oxygen electrode owing to the crossover of methanol (Murgia *et al.*, 2003). Consequently, the output cell voltage

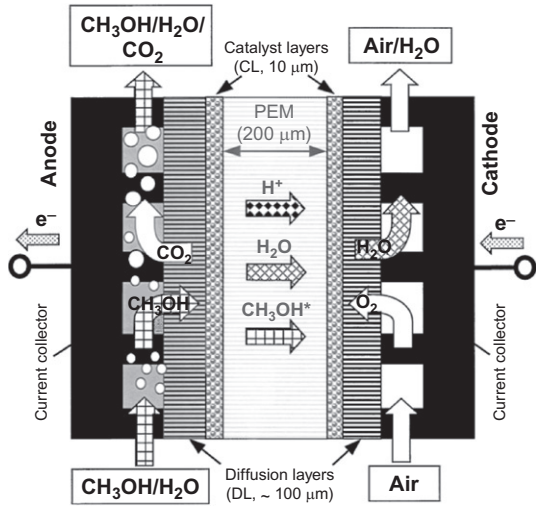

Figure 1 Schematic diagram of the DMFC with proton conducting membrane (CH_3OH^* = methanol crossover) (Sundmacher and Scott, 1999).

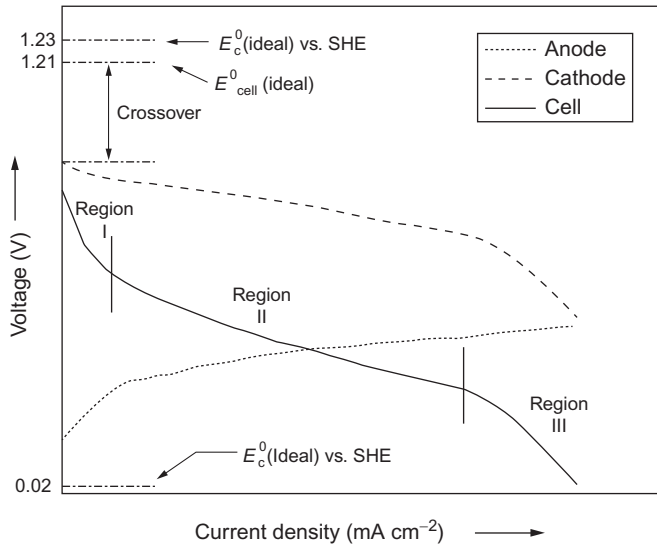

Figure 2 Polarization curves for a DMFC and its constituent electrodes (Murgia *et al.*, 2003).

in an SPE-DMFC is much lower than the ideal thermodynamic value, and it decreases with increasing current density as shown in Figure 2.

The operation of the DMFC can proceed with the feed either in the form of liquid or vapor. The vapor-feed system offers the attraction of better oxidation kinetics through higher temperatures and better gas phase mass transport. However, unless high fuel conversions are achieved in the cell, the system will be mechanically more complex through requirements to separate methanol (and water) from the carbon dioxide exhaust. Vapor phase operation also places additional heat-transfer requirements on the system, for example, to vaporize the aqueous fuel mixture. As a consequence, most DMFC development programs use liquid-feed systems which are mechanically simpler in terms of cooling and system thermal management. In liquid-feed systems, the exhaust from the anode is a two-phase mixture which requires condensation, or some other means of separation to remove methanol vapor from the carbon dioxide gas. An alternative method is to use a membrane gas separator.

2. PRINCIPLES OF OPERATION OF THE DMFC

2.1 Anodic oxidation of methanol

Generally speaking, the basic mechanism for methanol oxidation can be summarized in two functionalities, namely electrosorption of methanol onto an electrode substrate followed by addition of oxygen to adsorbed carbon-containing intermediates to generate carbon dioxide. In practice, only a few electrode materials are capable of adsorption of methanol and show good activity, for example, Pt (Kauranen *et al*., 1996) and platinum-based catalysts (Bagotzky and Vassilyer, 1967; Ley *et al*., 1997; Lizcano-Valbuena *et al*., 2002). On platinum, adsorption of methanol is believed to take place through a sequence of steps shown below. The first step is dissociative chemisorption of methanol onto the platinum surface, involving successive donation of electrons to the catalyst as follows (Kauranen *et al*., 1996):

$$\mathrm{Pt} + \mathrm{CH_3OH} \xrightarrow{k_1} \mathrm{Pt-CH_2OH} + \mathrm{H^+} + \mathrm{e^-} \quad (4)$$

$$\mathrm{Pt-CH_2OH} \xrightarrow{k_2} \mathrm{Pt_2-CHOH} + \mathrm{H^+} + \mathrm{e^-} \quad (5)$$

$$\mathrm{Pt_2-CHOH} \xrightarrow{k_3} \mathrm{Pt_3-COH} + \mathrm{H^+} + \mathrm{e^-} \quad (6)$$

where with the relative values of rate constants $k_1 < k_2 < k_3$ makes $\mathrm{Pt_3-COH}$ the major surface species.

Surface rearrangement of the oxidation intermediates generates carbon monoxide, linearly or bridge-bonded to Pt sites according to the reaction,

$$\mathrm{Pt_3-COH} \rightarrow \mathrm{Pt-CO} + 2\mathrm{Pt} + \mathrm{H^+} + \mathrm{e^-} \quad (7)$$

On Pt, water discharge occurs at high anodic overpotentials with the formation of Pt–OH species at the platinum surface.

$$Pt + H_2O \rightarrow Pt - OH + H^+ + e^- \quad (8)$$

The ultimate step is the reaction of Pt–OH groups with neighboring methanolic residues to give carbon dioxide according to the following reaction.

$$Pt - CO + Pt - OH \rightarrow 2Pt + CO_2 \uparrow + H^+ + e^- \quad (9)$$

Platinum however is not sufficiently active in methanol oxidation and can also lead to substantial organic by-products during methanol oxidation. Thus a promoter that could effectively provide oxygen in some active form to achieve facile oxidation of the chemisorbed CO on platinum is used. In the literature, various approaches toward platinum promotion have been attempted. The simplest method is to generate more Pt–O species on the platinum surface by incorporating certain metals with platinum to form alloys (e.g., Pt_3Cr and Pt_3Sn) which then dissolve to leave highly reticulated but active surfaces. A second approach is the use of surface adatoms produced by underpotential deposition on the platinum surface. A third type of promotion described in the literature is a combination of Pt with a base-metal oxide such as Nb, Zr, Ta, etc. A fourth type of promotion is the use of alloys of platinum with different metals such as Pt–Ru, Pt–Os, Pt–Ir, etc., where the second metal forms a surface oxide in the potential range for methanol oxidation. Among these, Pt–Ru alloy (Bagotzky and Vassilyer, 1967; Kauranen *et al*., 1996; Ley *et al*., 1997; Lizcano-Valbuena *et al*., 2002) has been found to be particularly effective, and efforts have been made to enhance the promotion on Pt–Ru-based ternary and quaternary alloys, for example, Pt–Ru–Os and Pt–Ru–Ir.

Pt–Ru and Pt–Sn alloys are the most widely studied catalysts (Aricò *et al*., 1994a,b; Bagotzky and Vassilyer, 1967; Kauranen *et al*., 1996), which strongly promote the oxidation of methanol and related methanolic species. On the Pt surface, during the methanol electro-oxidation at low potentials –CO groups are adsorbed while at high potentials chemisorption of –OH groups, takes place with both the processes succinctly separated. On a Pt–Ru surface, chemisorption of –OH groups shifts to lower potentials and overlaps with the region where –CO groups are adsorbed on the catalyst. On a Pt–Ru alloy, water discharge occurs on Ru sites at much lower potentials compared to pure Pt according to the reaction given below.

$$Ru + H_2O \rightarrow Ru - OH + H^+ + e^- \quad (10)$$

The final step is the reaction of Ru–OH groups with the neighboring methanolic residues adsorbed on Pt to be oxidized to carbon dioxide according to the reaction:

$$Pt - CO + Ru - OH \rightarrow Pt + Ru + CO_2 \uparrow + H^+ + e^- \quad (11)$$

Methanol oxidation is more facile on Pt–Ru and Pt–Sn surfaces because the reaction requires the electrocatalyst to be used in a potential regime where labile-bonded oxygen should be present on the surface. In this situation, the supply of active oxygen to the species is of paramount importance, since this, apparently, facilitates the oxidation of adsorbed methanolic residues to carbon dioxide. It has been documented that with the Pt–Sn alloy catalyst, promotion in methanol oxidation is seen in the low-potential region, while Pt–Ru is particularly active in the high-potential region. However, attempts to form a ternary Pt–Ru–Sn alloy led to expulsion of Ru.

2.2 Cathodic reduction of oxygen

Oxygen reduction reaction can proceed by two different pathways (Kordesch and Simader, 1994): namely, the direct four-electron pathway and peroxide pathway. The direct four-electron pathway in acidic medium proceeds as

$$O_2 + 4H^+ + 4e^- \rightarrow 2H_2O \, (E^0 = 1.23\,V \text{ vs. SHE}) \quad (12)$$

In an acidic medium, production of dioxygen through the peroxide pathway is possible as follows:

$$O_2 + 2H^+ + 2e^- \rightarrow H_2O_2 \left(E^0 = 0.67\,V \text{ vs. SHE}\right) \quad (13)$$

This is followed by either

$$H_2O_2 + 2H^+ + 2e^- \rightarrow 2H_2O \left(E^0 = 1.77\,V \text{ vs. SHE}\right) \quad (14)$$

or

$$2H_2O_2 \rightarrow 2H_2O + O_2 \quad (15)$$

The direct four-electron path does not involve the peroxide species and hence has a higher Faradaic efficiency in relation to the peroxide pathway. However, it has been difficult to find catalysts which could facilitate the direct four-electron pathway for dioxygen reduction. In addition to irreversible losses, there is an additional overpotential observed on the cathode due to methanol crossover in a DMFC (Heinzel and Barragán, 1999). Therefore, cathodes with high loadings of platinum are usually employed in SPE-DMFCs (Shukla *et al.*, 2002a). However, since platinum has a tendency to be poisoned with methanol, both methanol impermeable membranes and methanol-tolerant oxygen reduction catalysts are ideally required for practical realization of SPE-DMFCs. In recent years, certain Ru-based chalcogenides have shown promise as methanol-tolerant oxygen reduction catalysts (Murgia *et al.*, 2003; Shukla *et al.*, 2002b). However, these materials have much lower intrinsic specific activity for oxygen reduction than platinum.

2.3 DMFC materials and performance

One of the key problems impeding the development of DMFCs is the properties of the available proton-conducting membrane. Owing to the low reactivity of methanol as well as the low conductivity of commercially available proton exchange membranes, namely Nafion®, at ambient temperatures, it is preferred to have an operating temperature near 100°C for DMFCs. Nafion membranes need water inside their skeleton in order to exhibit good proton conductivity at such high temperatures. Although it is quite a difficult requirement for polymer electrolyte fuel cells, it is of little concern in SPE-DMFCs since water along with methanol is constantly circulated during operation. But the problem of methanol crossover associated with the Nafion membranes is detrimental to the performance of a DMFC since it reduces both the coulombic efficiency of the fuel cell and the cell voltage. Studies by Ren *et al*. (2000a) showed a crossover of methanol equivalent to 80 mA cm^{-2} at a load current density of 150 mA cm^{-2} using a Nafion membrane electrolyte in a liquid-feed DMFC at 80°C. Efforts have therefore been expended to develop methanol impermeable proton exchange membranes either by modifying the available Nafion membranes or by developing altogether new proton exchange membranes.

Previous research on the DMFC has almost unanimously concluded that perfluorinated polymer electrolytes give significantly better cell performance that the use of other (solution phase) electrolytes. Acid electrolytes such as triflic acid, perfluoroethane sulfonic acid, perfluoro-octane sulfonic acid and sulfuric acid are outperformed in terms of methanol oxidation by ionomer membranes such as Nafion® (Surampudi *et al*., 1994). It is interesting to note that the stoichiometric ratio of methanol to water is at a high concentration of methanol (~12M) which has rarely been considered in experimental cells. At such high methanol concentrations, good cell performance has not been achieved at present due to the problem of methanol crossover.

In general, the performance of the DMFC depends on the MEA construction method, the materials and the operating conditions in the cell. It is well documented that increasing cell temperature above approximately 60°C causes a significant increase in power performance and that, at 90°C and beyond, high power densities above 200 mW cm^{-2} are achievable. This power performance is typically achieved using pressurized oxygen or air at 2.0/2.5 bar pressure with catalysts of Pt–Ru (2.5 mg cm^{-2}) (Narayanan *et al*., 1995).

Low-temperature performance of the DMFC is particularly relevant to small scale and portable applications, where applications, energy density considerations are of major importance. The effective energy density of

methanol in a DMFC operating at 0.5V with 90% fuel efficiency is 2.25 $kWh\,kg^{-1}$. In comparison, for a hydrogen proton exchange membrane fuel cell (PEMFC) operating at 0.7V to achieve the same energy density requires a storage capability of >11% by weight, for example, as a metal hydride. This is a demanding requirement for the PEMFC, which does not have the advantage of using a liquid fuel.

Small scale-up of the DMFC is reported by Shukla *et al*. (1999) and Jung *et al*. (1998), Buttin *et al*. (2001) and Scott *et al*. (2000). Siemens, as part of a program to develop a 1-kW DMFC stack, reported data for a three-cell assembly with electrode areas of $550\,cm^2$. Operating on air (1.5bar), the cell gave 1.4V at $100\,mA\,cm^{-2}$ and delivered a power of 87W at 89A (Baldauf and Preidel, 1999). Jet Propulsion Laboratory (JPL) have reported performance data for a five-cell stack with electrodes of $25\,cm^2$ area (Valdez *et al*., 1997a). This stack gave a voltage of 2.2V at $100\,mA\,cm^{-2}$, at 60°C using air supplied at 23 times the stoichiometric excess. The Los Alamos laboratories developed DMFC stacks suitable for portable applications (Ren *et al*., 2000b). For a stack comprising five cells, $45\,cm^2$ area each, a power of 17W at approximately 10A, when operated at temperatures below 60°C and at ambient air pressure is reported. Scale-up of the DMFC has provided a stack of 30 cells with a peak power of 50W at 14V operating on 0.5M methanol at 60°C (Gottesfeld *et al*., 2000).

Small electronic devices require compact and lightweight power supplies, and DMFCs offer the potential for double the lifetime of lithium ion batteries. Fabrications of a micro-machined DMFC, using traditional micromachining techniques and macro-assembly based on silicon, have been demonstrated. Gold and aluminum can be deposited as a current collector (Stanley *et al*., 2002).

3. MATHEMATICAL MODELING OF THE DMFC

Modeling the DMFC can lead to a greater understanding of the cell and its interactions with other components in the system. Because of the similarities with the PEMFC, modeling of the DMFC using polymer electrolyte membranes (PEMs) can follow similar approaches to hydrogen PEM cells, although there are of course some crucial differences as will be discussed.

The DMFC consists of a thin composite structure of anode, cathode, and electrolyte. The electrocatalysts in a fuel cell are positioned on either side of the polymer electrolyte, to form the cell assembly. These electrocatalysts are supported on carbon and bonded using, typically Nafion®, ionomer. In this way, a three-dimensional (3D) electrode structure is produced in which electronic current movement is through the carbon support and ionic current flow is through the ionomer. The reactants are,

in practical operation, fed to the backsides of the electrodes. Flow fields are used to supply and distribute the fuel and the oxidant to the anode and the cathode electrocatalyst, respectively. The distribution of flow over the electrodes should ideally be uniform to try to ensure a uniform performance of each electrode across its surface. The flow field allows fluid to flow along the length of the electrode while permitting mass transport to the electrocatalyst normal to its surface.

In most practical systems, because single-cell potentials are small (<1 V) fuel cells are connected in series to produce useful higher overall voltages (Figure 3). Electrical connection in stacks is usually achieved using bipolar plates, which make electrical connection over the surface of the electrodes. A second function of the bipolar plates is to separate the anode and cathode fluids. These factors introduce several challenges in plate selection and design. For example, while the flow field enables access of gas to the electrode structure in its open spaces, it prevents electrical contact at these points. Electrical contact should be as frequent and as large as possible to mitigate against long current flow path lengths. However, large areas of electrical contact could lead to problems of access of reactant gases to regions under the electrical contact. Thus overall the flow field design and the flow therein are a critical factor in fuel-cell operation and modeling.

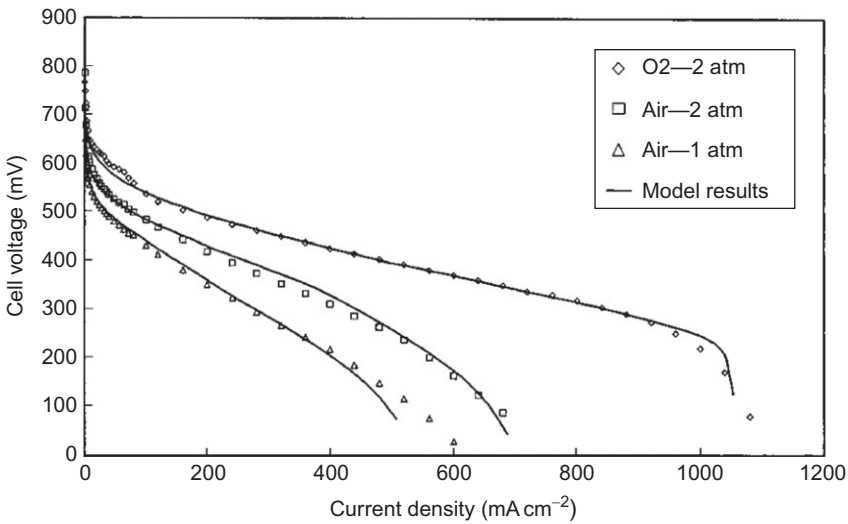

Figure 3 Cell polarization data obtained at 90°C for 1.5M aqueous methanol and the model results (Murgia *et al.*, 2003).

Overall modeling of the DMFC can occur at a series of different levels focusing on one or more different aspects or components in the cell as below:

(i) Anode catalysis. The mechanism of methanol oxidation is not known, but it is known that simple Butler–Volmer expressions are not appropriate.
(ii) PEM transport and conductivity. As well as facilitating proton transfer from anode to cathode the crossover of methanol and water is important in determining performance.
(iii) Cathode catalysis. Oxygen reduction is kinetically a faster process than methanol oxidation, but its overpotential behavior will have a significant influence on overall cell behavior. In addition, methanol oxidation at the cathode which through a mixed potential has severe repercussions on cell voltage.
(iv) Fluid transport in porous-backing layers. This influences the transport of reactants methanol and oxygen to the catalysts and the transport of products carbon dioxide and water away from the catalysts.
(v) Fluid mechanics in the flow channels. This impacts the local variation of methanol in the cell and is influenced by variations in velocity and pressure as also is the associated equilibrium between the methanol and water and carbon dioxide gas. This and many other factors will influence the current distribution over individual cells.
(vi) Current and potential distribution in the electrocatalyst layers. The electrodes in the DMFC are essentially 3D to provide a high specific area. The current is thus distributed in a direction normal to overall current flow, and this distribution should be determined for both the anode and the cathode.
(vii) Thermal energy and heat transfer. The electrochemical inefficient use of methanol leads to significant amounts of heat generation in the cell and thus local variations in temperature and heat-transfer rates may influence cell behavior.
(viii) Cell stacking. The practical application of multi-cell units requires, in principle, an integration of all the above factors. In addition, due regard must be taken of the variation in temperature in the cells and in the requirements of feeding air and methanol to the many compartments in the cell, that is, cell manifolds. Such behavior can see variations in performance from one cell to the other.
(ix) Dynamics. The application of the DMFC will inevitably impose a varied load demand on the unit, and the ability or not of the cell to respond effectively to the load demand will be crucial.

The types of models can vary from simple analytical and empirical models to detailed physicochemical models to stochastic models which cover single environments, such as electrodes, to complete fuel-cell systems.

Scott *et al*. (1997) developed a simple cell performance model describing mass transport in the porous electrode structures and the potential and concentration distributions in the electrode regions. The model incorporated the influence of methanol crossover based on a combination of diffusion, EOD, and pressure. Cruickshank and Scott (1998) presented a simplified DMFC model to predict the cell voltage characteristics depending on some key parameters obtained from measured permeation rates of methanol and water through Nafion® 117 membranes. Sundmacher and Scott (1999) developed a steady-state, isothermal cell model accounting for mass transfer and charge transport processes in the different fuel-cell layers. Kulikovsky (2002, 2003a,b) reported analytical models employing a semiempirical approach to account for the limiting current behavior. The general expression for the voltage–current curve is based on exact solution for the catalyst layer reaction and includes the overpotentials due to transport limitation in diffusion backing layer and due to methanol crossover.

The simplest DMFC performance models combine theoretical differential and algebraic equations with empirical determined parameters. However, the estimated parameters from the experimental data are normally specific to certain types of cells and valid for a limited range of operating conditions. The advantage of these models is their simple structure and the low computational effort to perform predictions for existing designs (Argyropoulos *et al*., 2003; Dohle and Wippermann, 2004; Kauranen and Skou, 1996; Simoglou *et al*., 2001a,b; Sundmacher *et al*., 2001).

Kauranen and Skou (1996) reported a DMFC model describing both the oxygen reduction and the methanol oxidation in the cathode and showed that the oxygen reduction current is reduced in the presence of methanol oxidation due to surface poisoning. Argyropoulos *et al*. (2003) presented a liquid-feed DMFC model to predict the cell voltage versus current density. The model is based on a semiempirical approach in which methanol oxidation and oxygen reduction kinetics are combined with effective mass transport coefficients for the fuel-cell electrodes. Dohle and Wippermann (2004) developed a DMFC model to predict polarization curves, and the permeability of methanol based on a set of parameters adjusted from experiments performed in a wide range of operating conditions.

3.1 Methanol oxidation

There have been various studies of the mechanism of methanol oxidation and several rate/kinetic models are proposed. It is generally thought that the rate-determining step is surface reaction between CO_{ads} and OH_{ads}. It has been proposed that methanol and hydroxyl groups are adsorbed on different parts of the surface on carbon supported platinum. Kaurenan and Skou (1996) developed a model for methanol oxidation on carbon supported platinum in which the rate of the surface reaction is limiting and that the hydroxyl adsorption is assumed in Nernstian equilibrium and followed a Langmuir adsorption. The rate of adsorption of the intermediate CO is expressed by a Temkin adsorption rate equation. CO and OH adsorption are assumed to occur at different sites of the supported catalyst. Observed experimental limiting currents are accredited to the adsorbed OH groups reaching saturation coverage. The model overall gave reasonable agreement with experimental observed anode polarization although aspects of methanol mass transport are not considered.

Nordlund and Lindbergh (2001) developed an agglomerate model for the porous DMFC anode using kinetic expressions for methanol oxidation based on the formation of adsorbed methanol, CO, and OH species. The transport of methanol in the spherical agglomerate is described by radial (Fick's) diffusion. It is shown that the mass transport does not limit cell performance but that liquid phase mass transport is of importance at lower methanol concentrations.

However, despite significant research on methanol oxidation, the mechanism is not fully known and the adsorption of the various reactive intermediates may involve a combination of single site and dual-site processes. These species may include those proposed in the mechanism of Freelink *et al*. (1996) for Pt alloys. Mayer and Newmann (2002a,c) have presented modeling and data analysis of transport phenomena in a SPE-DMFC. In contrast to most of the earlier models, which employ a simple Butler–Volmer (B–V) relationship for describing the electrode kinetics for methanol oxidation at the anode, the model due to Mayer and Newmann follows the reaction mechanism proposed by Gasteiger *et al*. (1995).

Scott and Argyropoulos (2004a,b) have proposed a one-dimensional (1D) potential distribution model of and used a kinetic model, derived from the adsorption model of Nordlund and Lindbergh (2001) using the stationary state approximation as follows:

$$j = \frac{6Fk_{10}c_{\mathrm{M}}\mathrm{e}^{\beta\eta}}{1 + k_{20}c_{\mathrm{M}}\mathrm{e}^{\beta\eta}} \tag{16}$$

However, it is important to state that the mechanistic model alone cannot generally be substantiated for porous high surface area

electrodes because of the influences of current distribution, variable geometry, and mass transport effects. Thus for modeling, electrode structure, and ionic and electronic conduction within, mass transport effects together with a kinetic model of the oxidation are required to predict electrode polarization and thereby cell voltage versus current density behavior.

3.2 Membrane transport

Characteristics of the PEM are critical in determining cell behavior. For the DMFC, the classic material used is the sulfonated perfluoropolymer sulfonic acid membrane, such as Nafion® from DuPont, Flemion® from Asahi Glass Co., and Aciplex® from Asahi Chem. Co., Ltd. The transport mechanisms of species such as water, methanol, and protons are important in building models that can predict the cell behavior. Springer *et al.* (1991) characterized the water transport through polymer membranes in terms of drag and diffusion coefficients. Bernardi and Vergrugge (1992) studied proton transport though the ionomer membrane and used a form of the Nernst–Planck equation that includes convection, diffusion, and migration. More comprehensive models of the transport processes have since been developed for ionomer membranes, for example, Um *et al.* (2000) and Gurau *et al.* (1998).

Verbrugge (1989) described a simple diffusion model of methanol transport through a PEM, assuming dilute solution theory. Validation of the model with experimental data showed that the diffusion rate of methanol through the membrane is nearly as fast as through water and Verbrugge (1989), from experimental and theoretical results, estimated the effective diffusion coefficient to be $1.15\times10^{-5}\text{cm}^2\text{s}^{-1}$ at 25°C for Nafion® 117.

Dohle *et al.* (2000) applied the method of Springer to the transport of water and methanol to model a vapor phase DMFC. Kulikovsky (2000) and Sundmacher (1999) used the Bernardi and Verbrugge model for transport in their DMFC model. The fluid velocity is expressed as a function of electro-potential and pressure using the Schogl's equation, and the flux of species is defined through the Nernst–Planck equation.

3.3 Effect of methanol crossover on fuel-cell performance

Operating parameters that affect methanol crossover are temperature, pressure, methanol concentration, membrane thickness, and current density. The influence of higher methanol concentration, and thus greater rates of methanol crossover, is expected to effects cell voltage in two ways:

reduction in the open-circuit voltage, that is, increased polarization at the cathode during practical operation and potentially a modification of the proton conductivity.

This experimental behavior has been simulated using a mixed potential model in which methanol oxidation and oxygen reduction occur simultaneously on the cathode. The presence of methanol has a significant effect in shifting the standard potential for oxygen reduction to lower values. It is also found that the cathode electrode performance is significantly lower at higher methanol concentration (Ravikumar and Shukla, 1996).

In general, increased methanol crossover is observed at higher temperature, in thinner membranes, at lower cathode side pressure and with higher methanol-feed concentrations. A simple empirical model of the water transport rates obtained by Ren *et al*. (1997) has been developed in which water transport is by either electro-osmosis or diffusion and electro-osmosis depending upon a critical current density.

In the DMFC, water transport is caused by three different factors, water required for the anode reaction, the electro-osmotic water transfer through the membrane with H^+ ions, and diffusion across the membrane. Water transfer starts at a finite value at zero current density (diffusion through the membrane) and rises relatively slowly with current density until a ''critical current density'' (i_{crit}) is reached, from where the water transfer increases linearly with current density. As load is applied to the cell, water accumulates in the cathode pores and the activity of the water effectively increases until the anode and cathode side water concentrations (or activities) are equal, after which the water transfer is by EOD. The total water transport (flux) across the membrane is given as

$$\begin{aligned} N_{\downarrow}(\mathrm{H_{\downarrow}2O})^{\uparrow} &= N_{\downarrow}(\mathrm{H_{\downarrow}2O})^{\uparrow} a + N_{\downarrow}(\mathrm{H_{\downarrow}2O}) \\ &= \{\blacksquare(i/6F + ((_{\downarrow}(\mathrm{H_{\downarrow}2O})i)/F + \vdash N_{\downarrow}(\mathrm{H_{\downarrow}2O}) \dashv|_{\downarrow}(i=0) \\ &-\left(D_{\downarrow}(\mathrm{H_{\downarrow}2O})^{\uparrow} m\right)/l_{\downarrow} m'' (''i \quad \text{if } i < i_{\downarrow}\text{crit@}i/6F + ((_{\downarrow}(\mathrm{H_{\downarrow}2O})i)/F\} \end{aligned} \tag{17}$$

where $(=\vdash N_{\downarrow}(\mathrm{H_{\downarrow}2O}) \dashv|_{\downarrow}(i{=}0)/i_{\downarrow}\mathrm{crit}\ l_{\downarrow} m/(D_{\downarrow}(\mathrm{H_{\downarrow}2O})^{\uparrow} m)$

The empirical model coefficients, (λ_{H_2O}), $N_{H_2O}|_{i=0}$ and i_{crit}, identified from data of Ren *et al*. (1997) are given by Scott *et al*. (1999a). The total methanol flow at the anode (reaction, diffusion, and electro-osmosis) is expressed as

$$N_{\downarrow}\mathrm{M}^{\uparrow} = i/6F + 18/(\rho_{\downarrow}(\mathrm{H_{\downarrow}2O})F)\,(_{\downarrow}(\mathrm{H_{\downarrow}2O})c_{\downarrow}\mathrm{M}^{\uparrow} a\, i + (D_{\downarrow}\mathrm{M}^{\uparrow} m)/l_{\downarrow} m \;\; c_{\downarrow}\mathrm{M}^{\downarrow} a \tag{18}$$

In this equation, methanol transfer flux in the MEA is brought about by reaction at the anode and transfer across the membrane by a combination of diffusion and EOD with water.

3.4 DMFC electrode modeling

To model the electrodes in the DMFC, a 1D model is typically used which contains the required elements of ionic transport, current flow, kinetics, and mass transport (Scott, 2003). For transport in a fuel cell, we in general must consider several interactive phenomena, which predict both dynamic and steady-state behavior. The governing equations for heat and material transfer in the diffusion and reaction layers, and electronic and ionic conduction are based on

(a) material balances of gases which take into account changes in gas voidage simultaneously with gas partial pressure and allow for a change in gas volume associated with a change in temperature;
(b) material balance of water and methanol vapor which include the influence of condensation or evaporation of water and methanol, depending upon the saturation partial pressure and the content of water in the vapor;
(c) material balance of liquid water (and methanol) which includes an appropriate description for the mechanism of water transport;
(d) energy balance of gas and solid phase which predict the local values of temperature;
(e) gas transport;
(f) the local values of current density as computed from an appropriate kinetic equation(s);
(g) variation in local potential and thus current density due to ionic (proton) conduction;
(h) electronic conduction in the catalyst and catalyst support solid phase;
(i) volumetric current balances.

In the development of a model, the following assumptions are frequently adopted: temperature of the gas phase is identical to the solid phase at every position and no heat transport in the gas phase. In a DMFC, oxygen reduction at the cathode leads to water formation which, if the gas phase is fully saturated, is present as liquid. This liquid phase can change the effective porosity of the diffusion layer by part filling the pores in which gas flows. This therefore influences the gas mass transport rate in the porous structure. The extent to which the porous structure is filled with liquid depends upon the governing mechanism for water transport through the structure. In addition, the transport of reactant gases and thus

local partial pressures are generally affected by Stefan–Maxwell diffusion, Knudsen diffusion, and friction pressure losses. Knudsen diffusion arises when the mean free path of the gas molecules is of a similar magnitude to the pore dimensions, that is, molecular and pore wall interactions. Pressure changes are due to friction and can be simply modeled on the basis of laminar flow in a capillary or Poiseuille flow.

The model of the gas flow field or porous diffusion layer cannot be considered in isolation as there is clearly significant interaction with the catalyst reaction layer and also the membrane in the fuel cell. In the case of the catalyst layer, the equations include chemical transformations associated with local reactions. The physicochemical effect of, for example, oxygen consumption and water generation affects the material balances of these two species and the energy balance. The diffusion layer is described by a set of differential equations, for gas and water transport, without the source term for material generation/consumption by electrochemical reaction.

3.5 Cell models

A simplified model of the DMFC has been developed by Scott *et al*. (1997) in which the diffusion of reactant methanol vapor and oxygen are modeled in terms of an effective diffusion coefficient and in which ion (proton) transfer is modeled by an effective conductivity in the structure. Solution of the model using Butler–Volmer kinetic equations for methanol oxidation and oxygen reduction gives the current distribution in the electrocatalyst layers, from which can be determined the overall electrode polarizations in the cell. In practice, this is an oversimplified picture of coupled reactant transport and ionic movement in catalyst layers which are covered with thin layers of ionomer (Nafion) and water.

Sundmacher and Scott (1999) and Scott *et al*. (1999b, 2001)) have developed several relatively straightforward models for single-phase and two-phase operation in liquid-feed cells and focused on the important influence of methanol diffusion which limits performance. Dohle *et al*. (2000) have developed a 1D model for the vapor-feed DMFC which included the effect of methanol concentration on the cell performance and methanol crossover.

A 1D model for predicting the cell voltage of the DMFC, which includes mass transfer behavior associated with the two-phase flow in the MEA diffusion layer has been produced (Scott *et al*., 1999b; Sundmacher and Scott, 1999). The two-phase flow model is based on capillary pressure theory and momentum balance equations for counter current gas and liquid flow and is used to determine the effective gas fraction in the porous layer. Agreement between the model and the

experiment is generally good over the full range of current densities. Clearly, the model is applied to the particular type of MEA used in this study, and it remains to be seen whether it can be used to predict behavior of other MEA structures and materials.

Sundmacher *et al*. (2001) studied both the static and the dynamic response of a SPE-DMFC and showed that methanol crossover in the cell can be reduced by pulsed methanol feed. Divisek *et al*. (2003) have also formulated a two-phase (water and gas) DMFC model using species and conservations equations as used by Wang and Wang (2001). In the model, the permeability of species is a function of ''capillary saturation'' which in turn depends on the capillary pressure. Mass transport between gas and liquid is modeled in terms of evaporation (or condensation) rates which are a function of surface area and temperature (Divisek *et al*., 2003).

A potential distribution model (Murgia *et al*., 2003) of a liquid-feed DMFC which accounts for two-phase flow and methanol crossover has been developed on the basis of Nernst–Planck equation, Stefan–Maxwell diffusion equations, and Butler–Volmer kinetics. The model of the anode and the fuel cell has been shown to give good agreement to experimental data. The model incorporates an approximate analytical integration of the Butler–Volmer equation over the catalyst layer to reduce the computational time required to solve the model. The model provides good predictions of anode polarization behavior and fuel-cell operating performance (Figure 3).

It is open to argument whether two-phase flow exists in the backing layers or especially in the catalyst layers. Gas formation will depend upon suitable conditions that facilitate gas bubble nucleation, in particular, capillary/pore size and wettability, but also the cell pressure, that is, carbon dioxide solubility. In fact, high-pressure operation has been suggested as one means of alleviating problems associated with gas evolution in the cell. In the absence of carbon dioxide gas, diffusion mass transport can be described by Stefan–Maxwell equations for the three components, namely methanol, water, and carbon dioxide.

Baxter *et al*. (2000) have developed a single-phase 1D model for the DMFC based on a simplified structure in which the anode comprises liquid-filled pores bounded by supported catalyst covered by a layer of ionomer. The model predicts that the variation of methanol in the anode catalyst layer is small and thus could lead to a simpler model than used by Baxter *et al*. (2000). Kulikovsky (2000) modeled a liquid-feed DMFC based on methanol transport through the liquid phase and in the hydrophilic pores of the anode-backing layer but ignored the effect of methanol crossover.

The flow in fuel and oxidant supply channels of fuel cells is usually laminar unless high stoichiometric excess of fuel or oxidant is used.

Hence, as an approximation, the flow in porous flow fields or in porous-backing layers can also be considered to be laminar. The influence of hydrodynamics in the flow fields is to change the local values of flow velocity, which has a direct influence on the mass transport or diffusion flux of species. In general, this variation in velocity occurs in three dimensions, which can result in a 3D variation in diffusion. Consequently, in the DMFC, we can expect that there will be multidimensional variation in local reactant gas partial pressure and thus local current density.

3.6 Two- and three-dimensional modeling

Wang and Wang (2001) have developed a two-dimensional (2D) model of a liquid-feed DMFC which includes diffusion and convection of gas and liquid phases in the backing layers and flow channels. The model allows for anode and cathode kinetics and methanol crossover. Anode kinetics is assumed to be zero order in methanol concentration. The influence of crossover is expressed as a parasitic current density, which affects both cell open-circuit potential and cathode kinetics. The model is validated against experimental data and notably predicts the observed limiting current behavior of the DMFC, which is said to be due to limited supply of oxygen at the cathode affected by methanol crossover.

A 3D, two-phase model is presented for DMFCs (Liu and Wang, 2007a), in particular, considering water transport and treating the catalyst layer explicitly as a component rather than an interface without thickness. Numerical simulations in 3D simultaneously solved flow, species, and charge-transport equations and explored mass transport phenomena occurring in DMFCs for portable applications. They revealed an interplay between the local current density and methanol crossover rate and indicate that the anode flow field design and methanol-feed concentration are two key parameters for optimal cell performance. Liu and Wang (2007b) presented a 3D two-phase DMFC model, which includes flow channels, backing and catalyst layers on both anode and cathode sides, and the membrane as a single simulation domain, that elaborates water transport. This model studied the net water transport coefficient distribution and interfacial liquid water coverage effect. Based on an interfacial liquid coverage model implemented in a 3D two-phase DMFC model, the liquid saturation variations in the cathode are examined in detail and their effects on the net water transport coefficient through the membrane described.

A 2D, two-phase mass transport model has been developed for a DMFC by He *et al*. (2009). The model is validated with published experimental data. In particular, gaseous and liquid phase velocities in the anode porous structure are obtained so that the liquid–gas counter

convection effect can be investigated. The numerical results show that the mass transfer of methanol is dominated by the resistance in the anode porous structure, which is affected by physical properties of the porous medium (porosity, permeability, and contacting angle). The cell performance can be improved by increasing the porosity and permeability, and decreasing the contacting angle of the porous medium for a given feed methanol concentration.

3.7 Nonisothermal modeling

In general, heat removal is a critical issue for fuel-cell operation. The electrochemical reactions taking place at a DMFC are exothermic and heat is also produced by irreversibilities in the cell (ohmic and activation losses). In principle, temperature profiles should be simulated in fuel-cell models although for single small cells this is often not done. Argyropoulos *et al*. (1999a,b) developed a thermal energy 1D mechanistic model for a DMFC stack based on the differential thermal energy equation.

A 2D, two-phase, nonisothermal model is developed for DMFC by Zou *et al*. (2010). The heat and mass transfer, along with the electrochemical reactions occurring in the DMFC, is modeled and numerically simulated. The model is able to predict cell performance under different operating conditions and can be used to investigate the effects of air and methanol-solution inlet temperature, MEA thermal conductivity, surrounding conditions and fuel inlet concentration on cell performance, methanol crossover, and the mean temperature and temperature difference in MEA.

Xu and Faghri (2010) developed a 2D, two-phase, nonisothermal model using the multifluid approach for a passive vapor-feed DMFC. The data showed that the passive vapor-feed DMFC, supplied with concentrated methanol solutions or neat methanol, can yield a similar performance with the liquid-feed DMFC fed with more dilute methanol solutions, while also showing a higher system energy density.

Reviews of DMFC modeling in the literature have previously been provided by Wang (2004) and Oliveira *et al*. (2007).

3.8 Dynamics and modeling

There is now some useful information published on the time-varying performance of the DMFC except with regard to stability studies. The effect of current pulsing on performance has been reported (Valdez *et al*., 1997b). More detailed studies of the dynamic voltage response under varied current loads have been also reported for small- and large-scale

cells (Argyropoulos *et al*., 2000, 2001) under a range of different operating conditions (see Figure 4). The cell responds rapidly and reversibly to changes in magnitude and rate of change of load. Under dynamic operation, the cell voltage response can be significantly better than that achieved under steady-state operation. Open-circuit potentials are also increased, by up to 100 mV, by imposing a dynamic loading strategy. In addition, the study reports the dynamic characteristics of a large-scale cell and cell stack and explains the differences in cell response.

Modeling of the dynamic behavior of the DMFC has been limited to only a few studies, although, in principle, most steady-state models can be readily adopted for dynamic simulation by introducing time derivatives. Dynamics are important from the point of assessing cell and system stability to fluctuation in variables as well as control. Sundmacher and Schultz *et al*. (Sundmacher *et al*., 2001) have extended their steady-state models to simulate dynamic operation. Through simulation of the pulsing of methanol-feed solution concentration, it is shown that an enhanced cell response (increased cell potential) is maintained as shown in Figure 5. This enhancement, confirmed experimentally, is due to the reduction in the impact of methanol crossover on oxygen reduction. The dynamic model is also used to simulate the operation of the DMFC in a vehicular application.

An empirical model based on a canonical variate analysis (CVA) state space representation has also been developed to predict the dynamic voltage response of the DMFC and multi-cell stacks (Simoglou *et al*., 2001a,b). In order to achieve high performance control of a commercial system, it is essential to have a methodology that will accurately predict the stack voltage from a minimum number of sensors and with the smallest time delay after vehicle's start-up. The advantage of CVA state space modeling is that no *a priori* knowledge of the system parameters,

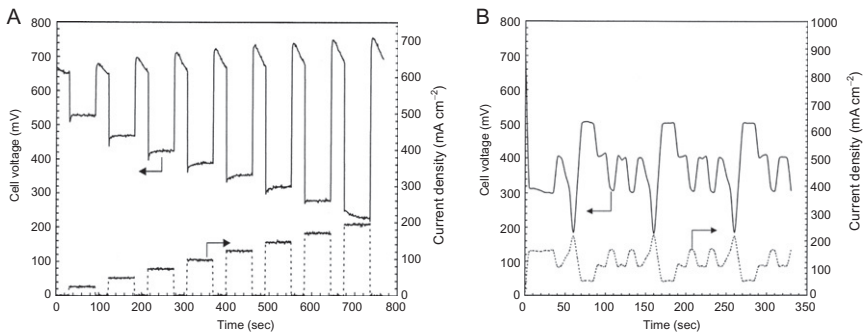

Figure 4 Dynamic response of small single DMFC cells under variable load conditions (Argyropoulos *et al*., 2000).

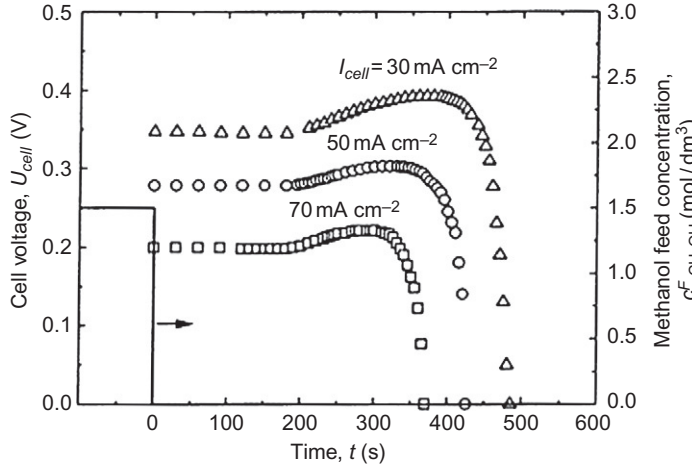

Figure 5 The effect of pulsed methanol-solution flow on DMFC performance (Sundmacher *et al*., 2001).

dynamics, or time delays is required. The CVA approach is able to describe with high accuracy (typically above 90% without model optimization) the system dynamics using only two measurement sources and provided acceptable inferential and one step ahead predictions even when the systems are operated without having reached a steady state.

Although empirical and semiempirical models are useful in modeling, in general, it is important to establish models that incorporate the physics and chemistry of the system to enable good prediction of behavior over a broad range of parameters and variables. Krewer *et al*. (2004) investigate the performance of a liquid fed rhomboidal DMFC anode compartment by experimental measurements and by 3D numerical simulations. The research focused on the residence time distribution (RTD) and the concentration distribution inside the compartment. Experimentally obtained RTD results and experimentally obtained concentration distribution inside the anode flow bed are in good agreement with the numerical simulations.

A dynamic model for a DMFC and its ancillary units is presented, by Zenith and Krewer (2010), in which all ancillary system's losses and main dynamics (cathodic oxygen fraction, anodic methanol concentration, stack temperature, system water holdup) are analyzed. The system is found to be stable in all of its dynamics except for that of water holdup. The influence of external conditions, such as temperature and humidity, on system feasibility is analyzed, and the capability of the system autonomous operation is found to depend essentially on environmental conditions and on the

chosen air excess ratio. System simulations confirmed the performance of the proposed controllers and their ability to stabilize water holdup.

A new structure of passive DMFC with two methanol reservoirs separated by a porous medium layer is mathematically modeled by Cai *et al*. (2011). The passive DMFC can be directly fed with highly concentrated methanol solution. The porosity of the porous medium layer is optimized using the proposed model. The new designed DMFC can be continuously operated for about 4.5 times longer than a conventional passive DMFC with the optimum parameters. The methanol crossover during the same discharging is only about 50% higher. The corresponding cell voltage variations obtained by both experimental measurement and numerical calculation, shown in Figure 6, show good agreement. The higher operation current density is used, and the shorter discharging time and lower cell voltage can be obtained. With a current density of $100\,mA\,cm^{-2}$, the H-DMFC is continuously operated for more than 10 h.

Gerteisen (2011) presented a dynamic model to investigate the coupled reaction mechanisms in a DMFC and therein associated voltage losses in the catalyst layers. The model accounted for the crossover of both methanol from anode to cathode and oxygen from cathode to anode. The reactant crossover results in parasitic internal currents that are finally responsible for high overpotentials in both electrodes, so-called mixed potentials. A simplified and general reaction mechanism for the methanol oxidation reaction (MOR) is selected, that accounts for the coverage of

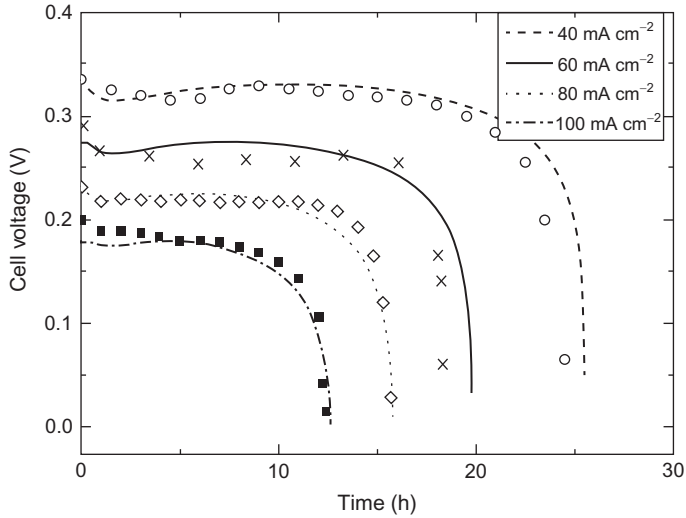

Figure 6 Evolution of cell voltage at different operation current densities (Cai *et al*., 2011).

active sites by intermediate species occurring during the MOR. The simulation of the anode potential relaxation after current interruption shows an undershoot behavior as seen in the experimental data. The model helps explain that this phenomenon is due to the transients of reactant crossover in combination with the change of CO and OH coverages on Pt and Ru, respectively.

A nonisothermal dynamic optimization model of DMFCs is developed to predict performance with an effective optimum-operating strategy (Ko *et al*., 2008). Through dynamic simulations, the anode feed concentration is shown to have significantly larger impact on methanol crossover, temperature, and cell voltage than the anode and cathode flow rates. Optimum transient conditions to satisfy the desired fuel efficiency are obtained by dynamic optimization. In the developed model, the significant influence of temperature on DMFC behavior is described in detail.

A 1D rigorous process model of a single-cell DMFC is presented by Shultz and Sundmacher (2011). Multicomponent mass transport in the diffusion layers and the PEM is described using the generalized Maxwell–Stefan (MS) equation for porous structures. Local swelling and nonidealities are accounted for in the PEM by a Flory–Huggins model for the activities of the mobile species inside the pores of the PEM. The two-phase behavior in both diffusion layers is neglected. The model showed good agreement to experimental data over a wide range of operating conditions, with respect to methanol and water crossover fluxes and current–voltage characteristics.

In the DMFC, there can be an increase in the transient cell temperature, driven by the waste heat that is generated for DMFC operation. This can be beneficial for cell performance through increased kinetics and mass transport, but the temperature rise also increases the amount of methanol crossover from the anode to the cathode, which causes high mixed cathode overpotential and ultimately lowers the overall DMFC efficiency. A transient-thermal model based on a lumped system is developed and implemented in a 1D, two-phase DMFC model (Chippar *et al*., 2010). The main focus is investigation of the transient-thermal behavior of DMFCs and its influence on methanol crossover, cell performance, and efficiency. 1D simulations are carried out, and the time-dependent thermal behaviors of DMFCs are analyzed for various methanol-feed concentrations and external heat-transfer conditions. The close interactions between the evolution of the transient temperature, methanol crossover, cell voltage, and efficiency during DMFC operations indicate that insufficient cooling of DMFCs can eventually lead to thermal runaway, particularly under high methanol-feed concentrations. Hence an efficient cooling system is needed to safeguard DMFC operations and enhance the performance of DMFCs for portable DMFC applications. In particular, as either a high methanol-feed concentration or/and low external heat-transfer coefficient is applied to a DMFC, the present model successfully captures the

thermal runaway phenomenon of DMFCs. This refers to a situation where an increase in the cell temperature enhances the rate of methanol crossover that causes a further increase in the temperature and results in a destructive DMFC operation.

An unsteady-state model is developed for a liquid-feed DMFC delivery considering two-phase system (Basri *et al.*, 2009). The model considered the mass and heat transport in the feed delivery system attached to the anode and cathode of the fuel cell. The unsteady-state model results are compared with the experimental data from in-house fabricated DMFC.

When DMFCs are used for portable power sources, it is impossible to keep the cell temperature constant, and thus it is important to know the cell performance at varying cell temperatures. Wang *et al.* (2006) examined experimentally the dynamic response of a DMFC to variable loading conditions. They analyzed the effect of cell temperature and oxygen flow rate on the cell response, and the cell response to continuously varying cell temperatures. The cell responded rapidly to variable current cycles and to continuously varying cell temperatures. An increased rate of gradual loading significantly influenced the dynamic behavior. The effects of cell temperature and oxygen flow rate on the cell dynamic responses are considerable, but the cell voltage differences over the range of cell temperatures and oxygen flow rates are small for gradual loading. The cell response to continuously varying cell temperature is depicted in Figure 7. The cell is heated to a value of temperature about 72°C. Then the heating is removed and the cell is cooled in static air. The cell is continuously operated, and the cell voltage responded quickly to cell temperature and followed the cell temperature. However, the open-circuit voltage during decreasing cell temperature is about 20 mV lower than that at the same cell temperature during increasing cell temperature.

A dynamic nonlinear circuit model for passive methanol fuel cells is presented by Guarnieri *et al.* (2010). The model takes into account mass transport, current generation, electronic and proton conduction, methanol adsorption, and electrochemical kinetics. Adsorption and oxidation rates, which mostly affect the cell dynamics, are modeled by a detailed two-step reaction mechanism. A fully coupled equivalent circuit is solved by assembling first-order differential equations into a nonlinear state-variable system in order to simulate the electrical evolution of the fuel cell from its initial conditions. The runtime of a DMFC can be predicted from the current load and the initial methanol concentration. The model shows that the fuel-cell dynamics over short and long timescales is dominated by mass transport in the diffusion layers and in the PEM and by electrochemical effects in catalyst layers and TPBs.

Dargahi and Rezanezhad (2009) considered the dynamic behavior of a DMFC-battery hybrid power source. Considering the limited ability of the DMFC system to produce power and importance of optimum methanol

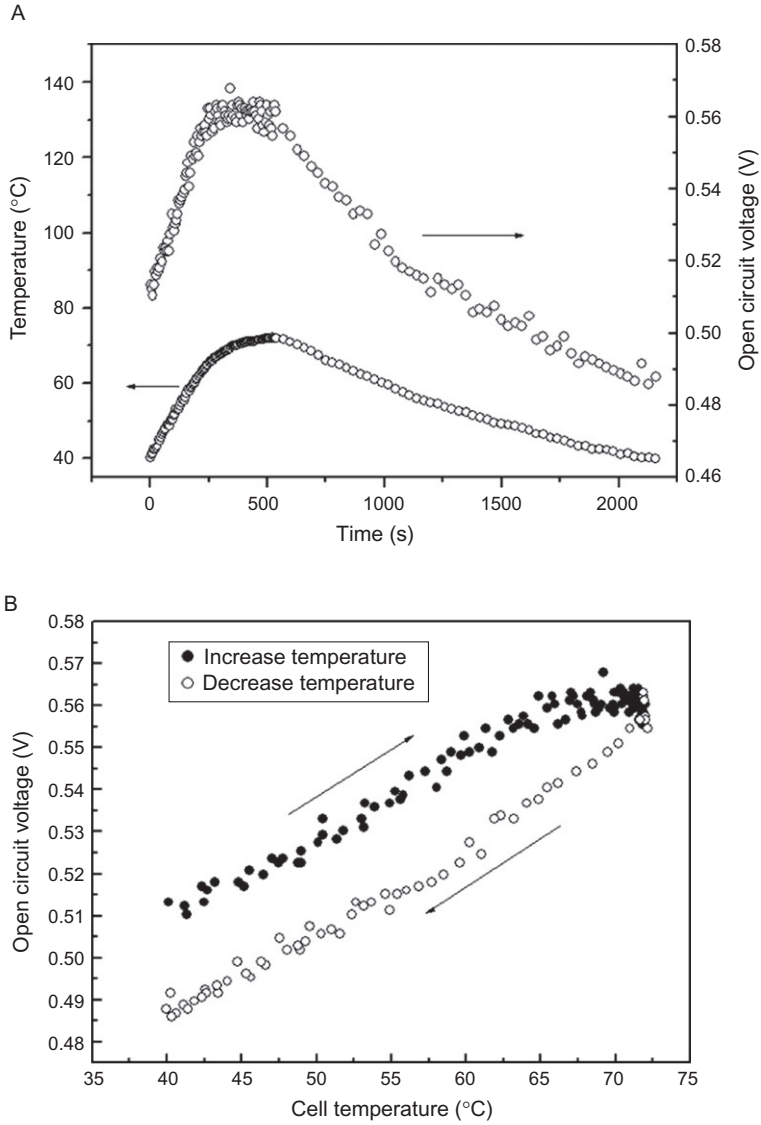

Figure 7 Cell open-circuit voltage response to continue change of cell temperature (Wang *et al*., 2006).

consumption, it is considered important to attain conditions, in which the maximum power of DMFC from the fuel flow can be used. A control scheme for DMFC/battery hybrid power system is proposed and analyzed.

4. MODEL OF THE DMFC POROUS ELECTRODE

The polarization, which quantitatively indicates the kinetic resistance, of the DMFCs is much higher than that of PEMFCs due to sluggish oxidation of methanol at the anode (García and Weidner, 2007; Gottesfeld, 2007; Meyers and Newman, 2002b; Scott and Shukla, 2007). As a result, porous electrode structures are used to support high current densities at low polarization, although typically current and overpotential are nonuniform due to the influence of mass and charge transfer in the structure (Newman, 2004; Newman and Tobias, 1962; Scott and Sun, 2007).

Meyers and Newman (2002b) developed a comprehensive model which describes the thermodynamics, transport phenomena, and electrode kinetics of the system in DMFC. The transport is described by concentrated-solution theory, and the electrochemical potential driving forces are described by a thermodynamic framework in which the equilibrium of species in a multi-component membrane is developed.

García *et al.* (2004) presented a 1D semianalytical model which can be solved rapidly so that it is suitable for inclusion in real-time system level DMFC simulations. This model accounted for the kinetics of the multistep MOR at the anode. Diffusion and crossover of methanol are modeled, and the mixed potential of the oxygen cathode due to methanol crossover is included.

Nordlund and Lindbergh (2002) adopted a porous model with agglomerates and kinetic equations based on surface coverage to study the influence of porous structure on the DMFC anode. The model indicated that mass transport limitations in the agglomerates are small and that the anode model can be simplified. However, the mass transport limitations in the liquid phase are of importance at lower methanol concentrations.

Scott and Argyropoulos (2004a,b) developed a 1D model of the current distribution in the anode of DMFC, which can be solved analytically. The model is applicable to an anode based on a metal mesh-supported electrocatalysts structure in which methanol oxidation is described by dual-site mechanism involving adsorbed CO and OH intermediates. The concentration of methanol is shown to influence overall electrode polarization characteristics, and critically the selection of the mechanism for methanol oxidation had a major impact in this respect.

In this model described here, the dual-site methanol oxidation mechanism (Shivhare *et al.*, 2006, 2007) is combined with material and charge balances (Scott and Sun, 2007; Sun, 2007; Sun and Scott, 2004a,b; Sun and Xing, 2009) to simulate the porous anode behavior and predict the effect of methanol concentration and temperature on anode polarization. Figure 8 is the modelling domain of the DMFC anode. In this model, the

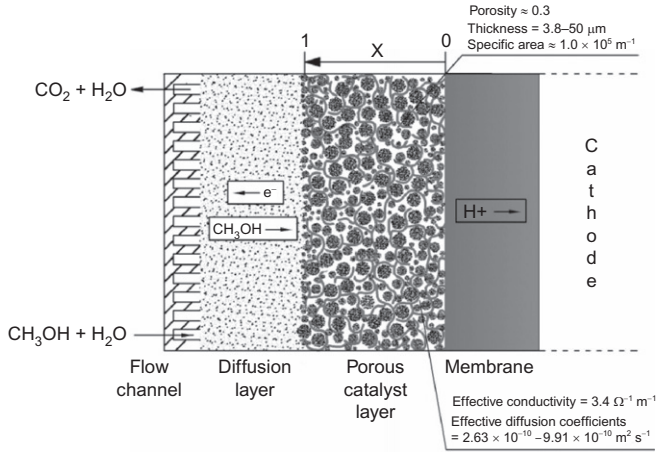

Figure 8 Scheme of the porous anode in DMFC (Sun *et al.*, 2010).

influence of CO_2 bubbling is omitted, although it is indeed difficult to avoid the effect of two-phase flow in the diffusion layer and flow channel to analyse the whole DMFC.

The assumptions adopted in the present model are as follows:

(1) Methanol concentration is defined as constant at the interface of catalyst layer (X=1). This meant that at the interface of catalyst layer, the methanol concentration is the same as the bulk concentration in the anode liquid channel.
(2) Carbon dioxide bubbles are formed beyond the catalyst layer. It is possible for nucleation of carbon dioxide to take place in diffusion layer or limited to a partial region of the catalyst layer by choosing appropriate operating condition (Scott *et al.*, 1999a,b).
(3) The porous catalyst layer is assumed to be isothermal, isotropic, and homogeneous.

4.1 Dual-site mechanism for methanol oxidation

According to dual-site kinetics which is widely accepted for methanol absorption and electrochemical oxidation on the surface of Pt–Ru catalyst, the methanol oxidation mechanism can be described as following four elemental steps:

$$CH_3OH \underset{k_1}{\overset{k_1}{\leftrightarrow}} CH_3OH_{ads} \tag{19}$$

$$CH_3OH \xrightarrow{k_2} CO_{ads} + 4H^+ + 4e^- \tag{20}$$

$$H_2O \underset{k_{3,1'}}{\overset{k_{3,1}}{\leftrightarrow}} OH_{ads,Ru} + H^+ + e^- \tag{21.1}$$

$$H_2O \underset{k_{3,2'}}{\overset{k_{3,2}}{\leftrightarrow}} OH_{ads,Pt} + H^+ + e^- \tag{21.2}$$

$$CO_{ads} + \left(OH_{ads,Pt} + OH_{ads,Ru}\right) \underset{k_4}{\overset{k_4}{\rightarrow}} CO_2 + H^+ + e^- \tag{22}$$

It is assumed that steps (19), (20), and (21.2) occurred on platinum sites (Pt), step (21.1) occurred on ruthenium sites (Ru) and step (22) is catalyzed on the sites of both Pt and Ru. Generally, it is believed that the reaction of CO_{ads} to CO_2 occurs on Ru sites. Pt sites serve as an active surface of adsorption and dehydrogenation of methanol (Gasteiger *et al.*, 1995, 2003; Kauranen and Skou 1996; Kauranen *et al.*, 1996). As a result, the rate-controlling step is reaction (22), which in turn depended on elemental steps (19–21.2) for the formation of adsorbed intermediates. Thus, the rate expression of the overall reaction can be written as

$$r_4 = k_4\theta_{OH,Pt}\,\theta_{CO,Pt}\exp(\beta E) + k_4\theta_{OH,Ru}\,\theta_{CO,Pt}\exp(\beta E) \tag{23}$$

where

$$\beta = \frac{(1-\beta_3)F}{RT} = \frac{(1-\beta_4)F}{RT} \tag{24}$$

The rates of changes of surface coverage of different intermediates with respect to time are as follows:

$$\Gamma\frac{d\theta_M}{dt} k_1 c_M\left(1-\theta_{OH,Pt}-\theta_{CO,Pt}-\theta_M\right) - k'_1\theta_M - k_2\theta_M e^{\left(\alpha_2 FE/R_gT\right)} \tag{25}$$

$$\Gamma\frac{d\theta_{CO,Pt}}{dt} = k_2\theta_M e^{\left(\alpha_2 FE/R_gT\right)} - k_4\theta_{OH,Pt}\theta_{CO,Pt}e^{\left((1-\beta_4)FE/R_gT\right)} - k_4\theta_{OH,Ru}\theta_{CO,Pt}e^{\left((1-\beta_4)FE/R_gT\right)} \tag{26}$$

$$\Gamma\frac{d\theta_{OH,Ru}}{dt} = k_{3,1}\,\alpha_{H_2O}(1-\theta]_{OH,Ru}[\square)e^{\left((1-\beta_3)FE/R_gT\right)} - k'_{3,1}\theta_{OH,Ru}\theta_{CO,Pt}e^{\left(-\beta_3 FE/R_gT\right)} - k_4\theta_{OH,Ru}\theta_{CO,Pt}e^{\left((1-\beta_4)FE/R_gT\right)} \tag{27}$$

$$\Gamma\frac{d\theta_{OH,Pt}}{dt} = k_{3,2}\,\alpha_{H_2O}(1-\theta]_{OH,Pt} - \theta_{CO,Pt} - [\theta_M)e^{\left(\frac{(1-\beta_3)FE}{R_gT}\right)} - k'_{3,2}\theta_{OH,Pt}\theta_{CO,Pt}e^{\left(\frac{-\beta_3 FE}{R_gT}\right)} - k_4\theta_{OH,Pt}\theta_{CO,Pt}e^{\left(\frac{(1-\beta_4)FE}{R_gT}\right)} \tag{28}$$

Numerous papers indicated that OH_{ads} is preferentially formed on the surface of Ru, not on the surface of Pt (Gasteiger *et al.*, 2003; Kauranen *et al.*, 1996; Krewer *et al.*, 2006; Schultz *et al.*, 2001). The previous modeling (Sun and Xing *et al.*, 2009; Sun *et al.*, 2010) confirmed that $\theta_{OH,Pt}$ is almost zero when the overpotential is lower than 0.5V (vs. dynamic hydrogen electrode (DHE)). As a result, it is reasonable to assume adsorption of hydroxyl ions on Pt sites could be neglected ($\theta_{OH,Pt}$=0). Thus, if the water activity can be defined as unity (a_{H_2O}=1), Equation (23) is simplified to

$$r_4 = k_4\theta_{OH,Ru}\theta_{CO,Pt}\exp(\beta E) \tag{29}$$

where $\theta_{OH,Ru}$ and $\theta_{CO,Pt}$ can be obtained from the result of solving Equations (25)–(27).

Intrinsic kinetic current density can be obtained by combining Faraday's law:

$$i = nFr_4 = i_0\theta_{\mathrm{OH,Ru}}\theta_{\mathrm{CO,Pt}}\exp(\beta E) \tag{30}$$

where the exchange current density $i_0 = nFk_4$.

Hence, the relationship of $i - E$ is applied as intrinsic kinetic expression to calculate the polarization curves without the influence of physical parameters.

4.2 Macrokinetics model

Mass transport of methanol in porous catalyst layer can be described by Fick's first law as

$$\overrightarrow{N_{\mathrm{M}}} = -D_{\mathrm{e}}\nabla c_{\mathrm{M}} \tag{31}$$

Because the transport process of methanol in a differential volume of catalyst layer is only described by diffusion, the divergence of $\overrightarrow{N_{\mathrm{M}}}$ is written as

$$\nabla\overrightarrow{N_{\mathrm{M}}} = -D_{\mathrm{e}}\nabla\cdot\nabla c_{\mathrm{M}} = -D_{\mathrm{e}}\nabla^2 c_{\mathrm{M}} \tag{32}$$

According to a mass balance (Scott and Sun, 2007b; Sun and Scott, 2004a; Sun and Xing, 2009; Sun *et al.*, 2010),

$$\nabla\overrightarrow{N_{\mathrm{M}}} = R = -ar_4 \tag{33}$$

Combine Equation (32) and Equation (33), we have

$$\nabla^2 c_{\mathrm{M}} = \frac{a}{D_{\mathrm{e}}}k_4\theta_{\mathrm{OH,Ru}}\theta_{\mathrm{CO,Pt}}\exp(\beta E) \tag{34}$$

Equation (34) is used to describe the effect of concentration changes on polarization of anode.

The boundary conditions for the second-order differential equation above are as follows:

$$c_{\mathrm{M}}(x=0) = c_{\mathrm{M}}^0, \quad \frac{\partial c_{\mathrm{M}}}{\partial x(x=l)} = 0 \tag{35}$$

Charge transport of methanol in the porous catalyst layer can be described by Ohm's law as

$$\overrightarrow{i} = -\kappa_{\mathrm{e}}\nabla\phi^l \tag{36}$$

The divergence of $\overrightarrow{i}$ is written as

$$\nabla\overrightarrow{i} = -\kappa_{\mathrm{e}}\nabla\cdot\nabla\phi^l = -\kappa_{\mathrm{e}}\nabla^2\phi^l \tag{37}$$

According to a charge balance (Scott and Sun, 2007b; Sun and Scott, 2004a; Sun and Xing, 2009; Sun *et al.*, 2010),

$$\nabla\overrightarrow{i} = ai \tag{38}$$

The overpotential, E, is written as $E = \phi^m - \phi^l - \phi^0$ (Nordlund and Lindbergh, 2002; Sun and Scott, 2004a,b; Sun and Xing, 2009; Sun *et al.*,

2010). Both ϕ^m and ϕ^l could be considered as constant. Substitute Equation (37) into Equation (38), the differential charge balance which described the potential field in the porous anode becomes a nonlinear Poisson equation:

$$\nabla^2 E = \frac{a}{\kappa_e} i_0 \theta_{OH,Ru} \theta_{CO,Pt} \exp(\beta E) \tag{39}$$

Equation (39) is used to describe the effect of ionic resistance on anode polarization.

The boundary conditions for the second-order differential equation above are as follows:

$$E(x = 0) = E^0, \quad \frac{\partial E}{\partial x(x = l)} = 0 \tag{40}$$

Equations (34) and (39) could be generalized by dimensionless variables such as $C_M = \frac{c_M}{c_M^0}$, $\Psi = \frac{E}{E^0}$, $X = \frac{x}{l}$. As a result, the dimensionless equations are presented as below:

$$\nabla^2 C_M = s \cdot \theta_{OH,Ru} \theta_{CO,Pt} \exp\left(\beta E^0 \Psi\right) \tag{41}$$

$$\nabla^2 \Psi = \mu \cdot \theta_{OH,Ru} \theta_{CO,Pt} \exp\left(\beta E^0 \Psi\right) \tag{42}$$

For a 1D porous electrode (García *et al.*, 2004), Equations (41) and (42) become

$$\frac{\partial^2 C_M}{\partial^2 X} = s \cdot \theta_{OH,Ru} \theta_{CO,Pt} \exp\left(\beta E^0 \Psi\right) \tag{43}$$

$$\frac{\partial^2 \Psi}{\partial^2 X} = \mu \cdot \theta_{OH,Ru} \theta_{CO,Pt} \exp\left(\beta E^0 \Psi\right) \tag{44}$$

with boundary conditions:

$$c_M(X = 0) = c_M^0, \quad \frac{\partial c_M}{\partial X(X = 1)} = 0 \tag{45}$$

$$E(X = 0) = E^0, \quad \frac{\partial E}{\partial X(X = 1)} = 0 \tag{46}$$

where $s = \frac{a i_0 l^2}{n F D_e c_M^0}$ and $\mu = \frac{a i_0 l^2}{\kappa_e E^0}$.

The dimensionless modulus, s, in Equation (43) characterizes resistances of mass transport in the porous anode, and the dimensionless modulus, μ, in Equation (44) characterizes the relative resistance of charge transport when applying different overpotentials at the boundary X=0.

According to Ohm's law, the local current density described by concentration and charge flux is

$$i_{loc} = -nFD_e \frac{dc_M}{dx} = -\kappa_e \frac{dE}{dx} \tag{47}$$

Thus, the dimensionless current density is defined as

$$I_{loc} = -\frac{1}{s}\frac{dC_M}{dX} = -\frac{1}{\mu}\frac{d\Psi}{dX} \tag{48}$$

Equations (47) and (48) can be used to describe the current distribution in the anode catalyst layer. Then the relationship between i and I can be obtained by the expression of s and μ,

$$I = \frac{i}{ai_0 l} \tag{49}$$

We can derive the total current density as

$$i_T = ai_0 l I_T = -\frac{nFD_e c_M^0}{l}\left(\frac{dC_M}{dX}\right)_{X=0} = -\frac{\kappa_e E^0}{l}\left(\frac{d\Psi}{dX}\right)_{X=0} \tag{50}$$

This is the equation for predicting the macro current density of the anode. Here the relationship of $E^0 - i_T$ and $\Psi - I_T$ typically describes the apparent and dimensionless polarization curve. Effectiveness factor is introduced to evaluate the impact of physical parameters such as thickness and specific surface area of the catalyst layer, effective diffusion coefficient, and effective conductivity of the anode, and is defined as

$$(= (\text{apparent current density})/(\text{intrinsic current density}) = i_{\downarrow}T/ali \tag{51}$$

i, which is calculated by solving Equations (25)–(27), and is only the function of initial methanol concentration and overpotential c_M^0 and E^0.

Substituting Equation (30) into Equation (51), we obtain

$$\begin{aligned}&(= (\text{apparent current density})/(\text{intrinsic current density})\\ &= i_{\downarrow}T/\left(ali_{\downarrow}0\ \theta_{\downarrow}(\mathrm{OH,Ru})\ \theta_{\downarrow}(\mathrm{CO,Pt})\ \exp\left(\beta E^{\uparrow}0\right)\right)\\ &= I_{\downarrow}T/(\llbracket\theta_{\downarrow}(\mathrm{OH,Ru})\theta\rrbracket_{\downarrow}(\mathrm{CO,Pt})\ \exp(\phi^{\uparrow}0))\end{aligned} \tag{52}$$

Hence, the expressions of $(\llbracket -I\rrbracket_{\downarrow}T$ and $(-\Phi^{\uparrow}0$ are applied to calculate the effectiveness of the Pt–Ru catalyst layer. Assume that the thickness and width of the catalyst layer would be of the same order of magnitude. The modeling domain is chosen as a rectangle with the width five times larger than the thickness. The parameters used for the modeling are listed in Tables 1 and 2.

4.3 Coverage ratios of intermediate species

Generally, the superficial rate or current density is proportional to both coverage ratios $\theta_{OH,Ru}$ and θ_{co}, which are mutually coupled with the coverage ratio θ_M, of CH_3OH_{ads} adsorbed at Pt sites. Also all of the coverage ratios are functions of concentration, temperature, and overpotential.

Figure 9 shows the variations of surface coverage ratios with overpotential E, calculated by using the kinetics parameters at 30, 60, and 90°C with 1.0M of methanol. The values for θ_M and $\theta_{OH,Ru}$ are shown on the left y-axis, while values for θ_{co} are shown on the right y-axis with a scale of 10^{-5}.

With increase in overpotential, $\theta_{OH,Ru}$ rapidly increases to near 1, undergoes a slight decrease, and approaches 1 again. While θ_M initially maintains a value approximately that of the adsorption equilibrium, it later undergoes a sharp decrease, finally maintaining a small near

constant value. Simultaneously, θ_{co} first shows a sharp increase and then undergoes a sharp decrease, ultimately maintaining very small values. This means that the electrochemical formation of OH at Ru site (step (21.1)) may not become a rate-limiting step. Moreover, the adsorption rate of methanol (step (19)) is the rate-limiting step at high overpotentials, and the electrochemical dehydrogenation of CH_3OH_{ads} at Pt sites (step (20)) is considered as the rate-limiting step at low overpotentials.

In Figure 9, we can see that the greatest influence of temperature on the coverage ratios shown in the case with medium overpotential and that θ_{co} is more sensitive to temperature than the other two coverage ratios. Figure 10 shows the variation in surface coverage with potential at different concentrations at 60°C. The values of θ_M appear to be more sensitive, and the values of $\theta_{OH,Ru}$ and θ_{co}, less sensitive to concentration than to temperature. The rate-limiting step will be step (20) at low overpotential then changes to step (19) at high overpotential.

Table 1 Physical parameters used for the modeling

Electrode parameters	References
Catalyst layer thickness l (m)	
3.8×10^{-6}	Newman and Tobias (1962)
5.0×10^{-6}	Shao *et al.* (2006)
1.0×10^{-5}	Scott and Argyropoulos (2004a,b)
2.3×10^{-5}	Nordlund and Lindbergh (2002)
2.5×10^{-5}	Chan *et al.* (2006)
5.0×10^{-5}	Kauranen *et al.* (1996)
Specific area of anode a (m^{-1})	
118,317	Scott and Argyropoulos (2004a)
1.0×10^{5}	García *et al.* (2004)
Porosity of anode ε	
0.3	Scott *et al.* (1997)
Diffusion coefficients D_0 (m^2s^{-1})	
$2.8\times10^{-9}\exp[2436(1/353-1/T)]$	Scott *et al.* (1997, 1999a)
1.6×10^{-9} (70°C)	Nordlund and Lindbergh (2002)
6.03×10^{-9} (60°C)	Nordlund and Lindbergh (2004)
Effective diffusion coefficients D_e (m^2s^{-1})	
$D_e=D_0\varepsilon^{1.5}$	Newman (2004) and Nordlund and Lindbergh (2002)
Effective conductivity κ_e $(\Omega^{-1}m^{-1})$	
3.4	Scott and Argyropoulos (2004a,b)

Table 2 Kinetics parameters used for the modeling (Shivhare *et al*., 2006)

Kinetics parameters	303K	333K	363K
k_1 (ms^{-1})	8.7×10^{-7}	4.2×10^{-6}	1.0×10^{-5}
k_1^- ($molm^{-2}s^{-1}$)	4.0×10^{-4}	1.5×10^{-3}	2.6×10^{-3}
k_2 ($molm^{-2}s^{-1}$)	3.5×10^{-9}	9.5×10^{-8}	8.0×10^{-7}
$k_{3,2}$ ($molm^{-2}s^{-1}$)	4.0×10^{-5}	5.0×10^{-5}	6.0×10^{-5}
$k_{3,2}$ ($molm^{-2}s^{-1}$)	3.0×10^{-5}	1.8×10^{-5}	1.4×10^{-5}
k_4 ($molm^{-2}s^{-1}$)	5.3×10^{-2}	5.9×10^{-2}	6.2×10^{-2}
aH_2O	1.0		
a_2	0.79		
β_3 (V^{-1})	0.5		
β_4 (V^{-1})	0.5		

Overall, the rate-limiting step may change from step (20) which is independent of concentration to step (19) which is independent of overpotential. This leads not only to a change in apparent activation energy but also to a change of reaction order between 0 and 1 with respect to methanol concentration. Furthermore, it should be noted that θ_{co} cannot be neglected since it is proportional to the total reaction rate, although its values are quite small. The sharp change of θ_{co} as well as θ_M with overpotential is the reason that the kinetics of methanol oxidation on Pt–Ru cannot be simply described by B–V equations.

4.4 Distributions of concentration, overpotential, and current density

Figure 11 shows a set of representative dimensionless solutions, the values of kinetic parameters are adopted from reference (Shivhare *et al*., 2006), and modulus v^2=40.0 and s=25.0 are taken. The normalized $\Psi(X)$ and $C_M(X)$ are on the y-axis and the dimensionless distance X on the x-axis.

Generally, the distributions of overpotential are flatter than those of concentration since the conductivity of electrolyte is always good; however, their influence on apparent currents are often considerable due to the sensitivity of the overpotential. With increasing overpotentials, the distributions of concentration are steeper because of the increasing influence of diffusion in the pores. A minimum of $\Psi(X)$ appears near a value of Φ^0=8.0, and this unusual phenomena is caused by the mechanism of methanol oxidation on the Pt–Ru porous anode. Along with increasing

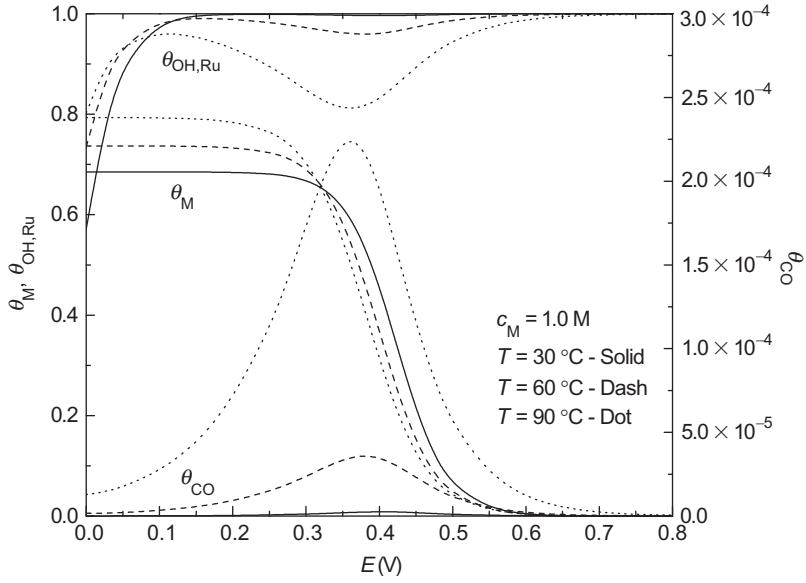

Figure 9 Variations of coverage ratios with overpotential at different temperatures (Sun *et al.*, 2010).

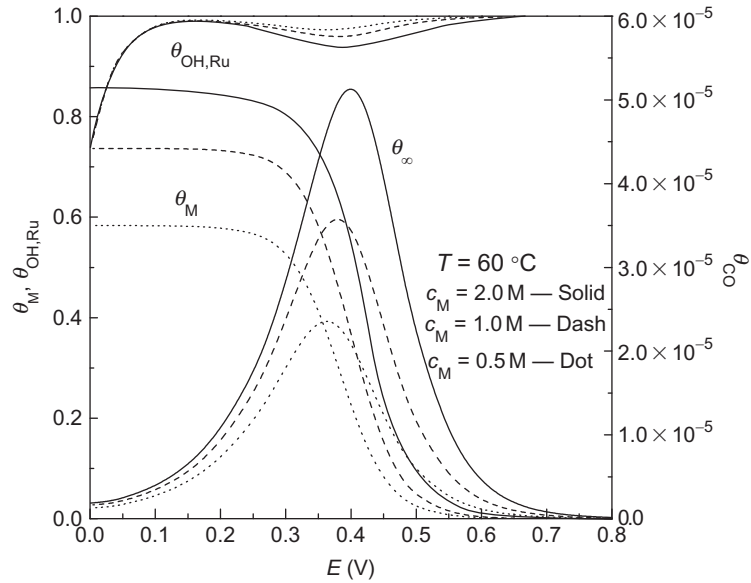

Figure 10 Variations of coverage ratios with overpotential at different methanol concentration (Sun *et al.*, 2010).

Φ^0, the influence of the element step of methanol chemical adsorption which is irrespective of potential on the intrinsic reaction rate becomes greater (Shivhare *et al.*, 2006) until the step becomes the rate-limiting one at Φ^0=8.0 (the minimum of $\Psi(X)$) or larger Φ^0.

Figure 12 shows the distributions of dimensionless current density with different thickness and specific area of the catalyst layer, operating temperature, methanol concentration, and overpotential of the catalyst layer. The dimensionless current and its nonlinearity increased with smaller thickness and specific area of the catalyst layer, higher operating temperature, overpotential, and larger methanol concentration. From Equation (49), the definition of the dimensionless current I, we can conclude that the dimensionless modulus s and μ, which are influenced by the change of the thickness and specific area of the catalyst layer, the operating temperature, the methanol concentration, and the overpotential affect the dimensionless current.

Apparently, an increase in operating temperature, methanol concentration, and overpotential increases the dimensionless current density. However, higher dimensionless current density is observed in the catalyst layer with smaller thickness and specific area. It is because of the higher utilization rate of the interface of the catalyst layer. Moreover, the

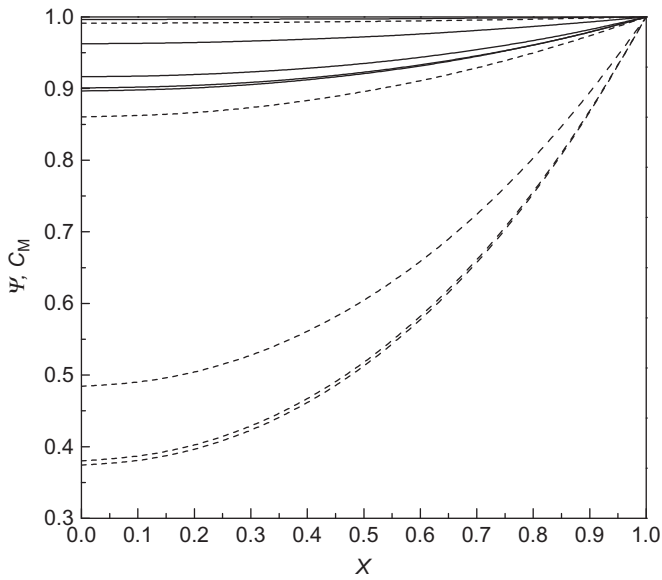

Figure 11 The distribution of dimensionless potential Ψ and dimensionless concentration C_M with different value of Φ^0, solid line: from up to down Φ^0=4.0, 6.0, 12.0, 10.0, 8.0 for Ψ; dash line: from up to down Φ^0=4.0, 6.0, 8.0, 10.0, 12.0 for C_M (Sun and Xing, 2009).

apparent current density (i_T) is observed in the catalyst layer with larger thickness and specific area because the apparent current density is determined not only by the dimensionless current density (I_T) but also by thickness (l) and specific area (a) as well as exchange current density (i_0) according to expression (50).

4.5 Polarization curves

Figure 13a shows examples of the polarization curves corresponding to physical parameters arranged into five groups by three levels of electrode thickness, two levels of specific area, and one level of effective diffusion coefficient. The parameters used for the curve numbered 4 are very close to those used in papers (Scott *et al.*, 1999b; Shivhare *et al.*, 2006). All the polarization curves possess the same trend, an approximate exponential rise in current density with increasing overpotential and eventually approaching a maximum current density. This maximum current density is an ''adsorption limiting current density'' which due to the limitation of species adsorption rather than the ''limiting current density'' caused by mass transport. The data show that thicker electrodes and higher specific electrode areas result in

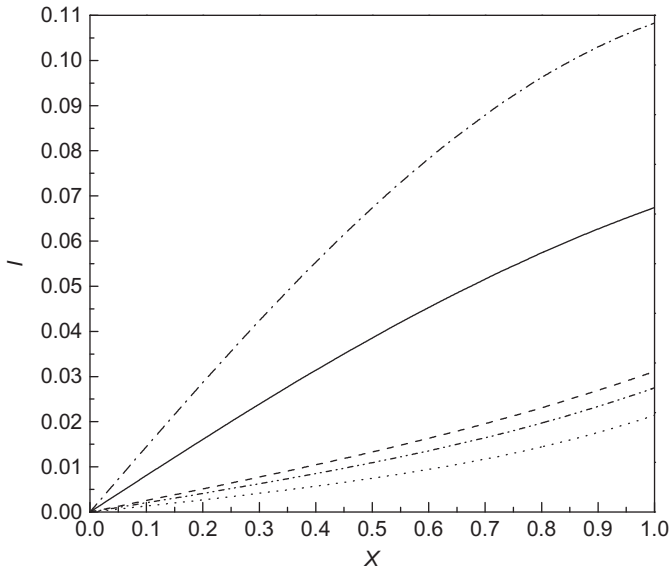

Figure 12 The distribution of dimensionless current with different thickness and specific area of catalyst layer: T=333K, C_M^0=1.0M, E^0=0.4V, κ_e=3.4Ω^{-1}m^{-1}, D_e=3.04×10^{-10}m^{2}s^{-1}; solid line: l=10μm, a=1.0×10^{5}m^{-1}; dash line: l=25μm, a=1.0×10^5 m^{-1}; dot line: l=50μm, a=1.0×10^{5}m^{-1}; dash dot line: l=10μm, a=1.0×10^{4}m^{-1}; dash dot dot line: l=10μm, a=1.0×10^{6}m^{-1} (Xing *et al.*, 2011).

higher current densities at a given potential. The current densities are determined by the very low dehydrogenation rate of step (20) at low overpotential as well as by the adsorption rate of step (19) at high overpotential.

Figure 13b shows the dimensionless polarization curves I–Φ^0 corresponding to the same physical parameters of Figure 13a, and thus the dimensionless values of v^2 and s. Current density is proportional to the mean value of current density per unit of inner surface area over the porous anode $i_T/(al)$, and therefore, the I–Φ^0 curve shows the effects of mass and charge transfer on the porous anode. The curve with symbols, which are calculated by the macrokinetic model with setting the catalyst layer as 10^{-8}m, represents the dimensionless intrinsic polarization curve independent of physical parameters. The decreasing values of v^2 and s corresponding to curves of 1, 2, 3, 4, and 5 result in higher current densities and indicate the decreasing influence of transport processes in the porous electrode. High values of v^2 and s ($\sim$40–50) for curve 1 have a large effect of transport, while low values ($<$1.0) for curves 4 or 5 near the intrinsic curve had a slight effect. The physical parameters used for curve 4 are close to those in papers (Scott *et al.*, 1999b; Shivhare *et al.*, 2006), which means that the kinetic experiments are carried out under approximate intrinsic conditions.

4.6 Effectiveness

The effects of mass and charge transport could be characterized by the effectiveness of the porous anode. The polarization curves, which are calculated corresponding to the physical parameters in Figure 13a, are shown in Figure 14a. The effectiveness is higher for thinner electrodes and higher specific areas due to the decreasing influence of mass transport processes.

With an increase in current density, every point of the porous anode can undergo a change of limiting step from step (20) to step (19), depending on the local concentration and overpotential at the point. Therefore, the end point of each curve represents the dimensionless adsorption limiting current density, where only the effect of mass transport exists since the limiting step (19) is independent of overpotential. The data with symbol overlapping curve 4 (Figure 14a) are calculated from the physical parameters used in paper (Scott *et al.*, 1996b; Shivhare *et al.*, 2006). Here all have values of effectiveness greater than 0.96, approaching a value of 1.0.

Theoretically, the effectiveness is a function of both the effective diffusion coefficient and conductivity characterizing both mass and charge transport in the porous anode. Figure 14b shows the variations of effectiveness with effective diffusion coefficients, which are corrected by Bruggeman equation (i.e., $D_{\downarrow}e = D_{\downarrow}0(^{\uparrow}1.5)$) (Newman, 2004; Nordlund and Lindbergh,

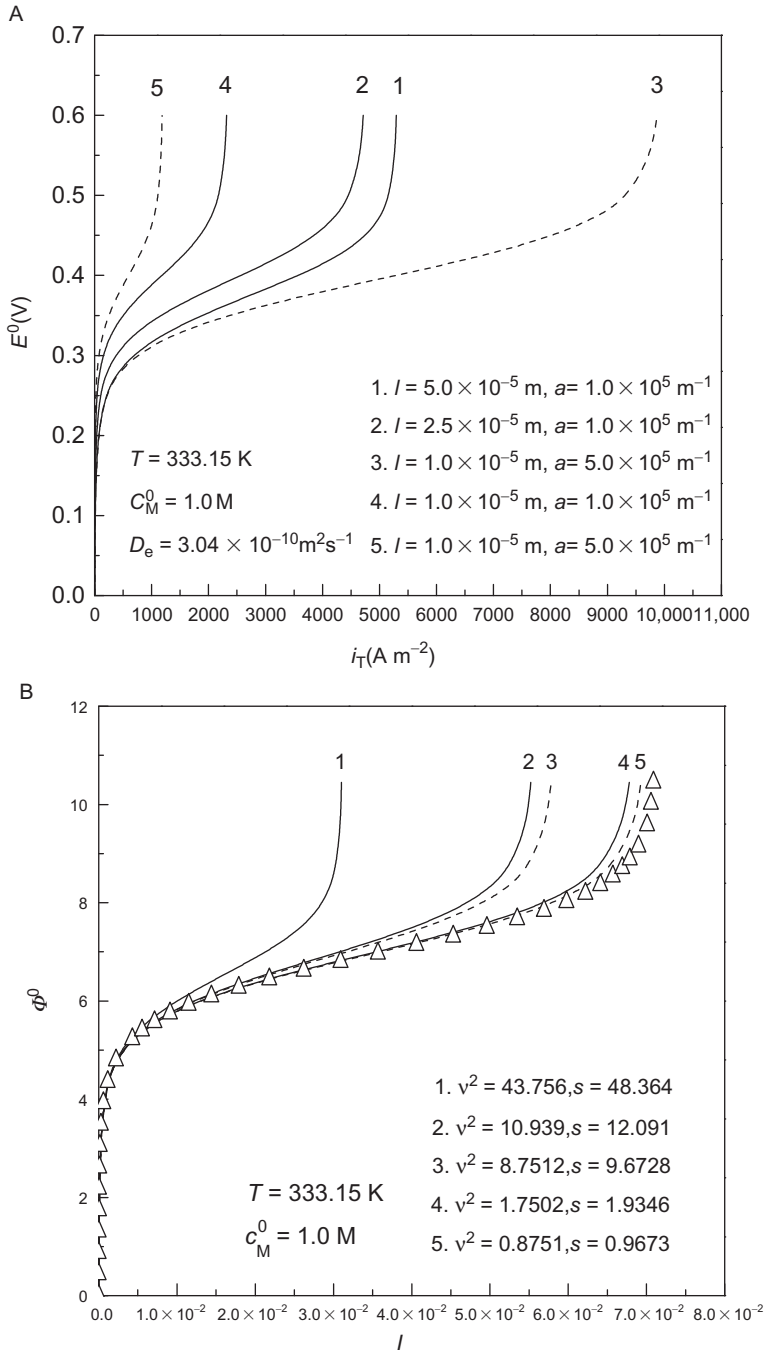

Figure 13 (a) Macropolarization curves of $i_T - E^0$ for different specific area and thickness. (b) Dimensionless macropolarization curves of $l - \Phi^0$ for different dimensionless modulus v^2 and s (Sun *et al.*, 2010).

2002), essentially consider the effect of porosity of the anode. The physical parameters are arranged into nine groups by three levels of electrode thickness, three levels of effective diffusion coefficient, and one level of specific area. The three groups of curves, for the same value of effective diffusion coefficient, show the effects of porosity and electrode thickness on effectiveness. The influence of pore diffusion becomes less significant while thinner porous electrodes as well as larger effective diffusion coefficients are applied. Then higher effectiveness values are achieved. Generally, effectiveness decreases with increasing current density.

However, effectiveness goes through a minimum with current density for thicker porous electrode and larger effective diffusion coefficient, which is caused by the effects of both mass and charge transport.

With unceasingly increasing current density, the effect of charge-transport resistance gradually disappears due to the change in the limiting reaction step from step (20) to step (19). The effect of better mass transport, which is caused by the larger effective diffusion coefficient, leads to a recovery of effectiveness while current density increases. This means that the electrode would be operated at or close to a limiting current, because more active sites of the electrode would be fully used, until adsorption limiting current density approached.

4.7 Model validation

The simulated polarization curves of the DMFC anode at different operating temperature and methanol concentration are shown in Figure 15. The kinetic parameters are selected from the paper of Shivhare *et al*. (2006). As shown in Figure 15, the simulated polarization curves are obtained by using two groups of thicknesses and specific areas of the catalyst layer selected from literatures (García *et al*., 2004; Kauranen *et al*., 1996; Scott and Argyropoulos, 2004a,b; Scott *et al*., 1999a,b; Shivhare *et al*., 2006; Sun and Xing, 2009; Sun *et al*., 2010).

Figure 15 indicates that the simulated polarization curves show good agreement with the experimental data at lower bulk concentration, lower operating temperature, and lower overpotential. Differences between the simulated values and experimental data become more apparent at higher bulk concentration, higher temperatures, and higher overpotentials, with the simulated values being higher than experimental values. The simulations overpredict the current densities of the fuel cell at the higher temperature and methanol concentration in comparison to experimental data. This may be due to liberation of carbon dioxide bubbles, which are generated by the increased electrochemical reaction and temperature (lower solubility), limiting methanol transfer from the bulk into the porous catalyst layer.

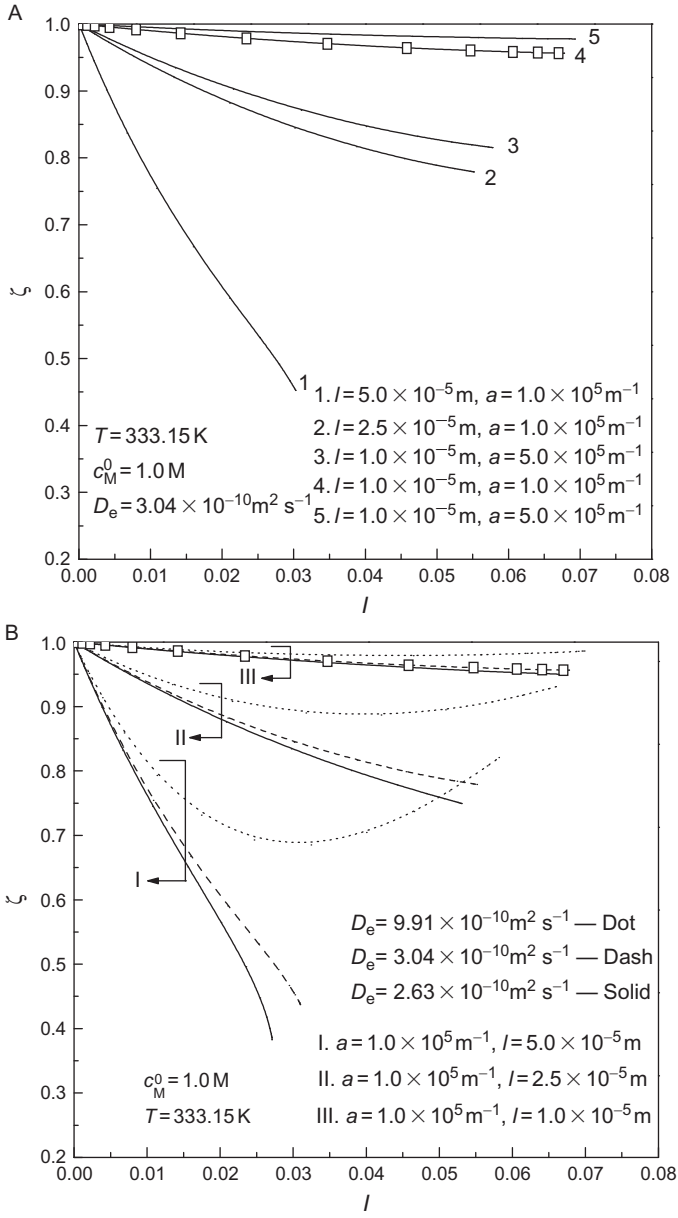

Figure 14 (a) Variation of effectiveness ζ with dimensionless current density I for different specific area a and thickness l; (b) variation of effectiveness ζ with dimensionless current density I for different thickness l and efficient diffusion coefficient D_e (Sun *et al.*, 2010).

5. DYNAMIC BEHAVIOR OF THE DMFC BASED ON A DUAL-SITE ELECTROCATALYST MODEL

For both the theoretical analysis and the practical operation of the DMFC, the open-circuit cell voltages (in the range of 0.6–0.7V) are much lower than the thermodynamically expected value which is around 1.2V. This is because of mechanism of methanol oxidation on Pt–Ru catalysts and due to methanol crossover. Higher output of the DMFC could be achieved by more selective catalysts, better membrane materials or by dynamic methanol-feeding strategies such as periodically pulsed methanol feeding (Sundmacher *et al.*, 2001).

As discussed in Section 4, the macrokinetics of methanol oxidation could be simplified to intrinsic when thinner electrode is applied. Based on the dual-site mechanism in Section 4.1, the time-dependent response of current density stimulated by overpotential could be calculated according to Equation (30). It is worthwhile to note that the intermediates such as θ_M, $\theta_{OH,Ru}$, and $\theta_{co,pt}$ are all related to temperature, methanol

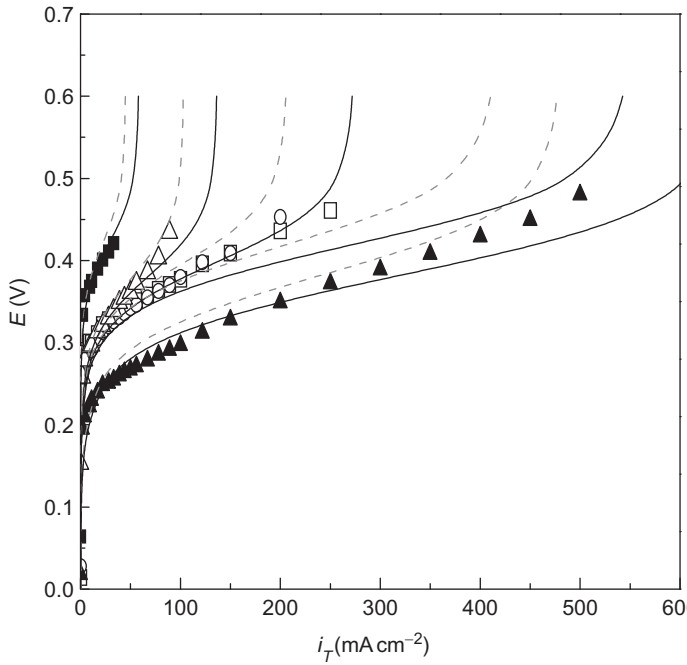

Figure 15 Comparison of calculated and experimental anode polarization data at various temperature and methanol concentration, κ_e=3.4Ω^{-1}m^{-1}, D_e=3.04×10^{-10}m^2 s^{-1}; experimental data: ■, C_M^0=1.0M, T=303K; ▲, C_M^0=1.0M, T=363K; △, C_M^0=0.5M, T=333 K; ○, C_M^0=1.0M, T=333K; □, C_M^0=2.0M, T=333K; simulation results: solid line: l=10μm, a=118,317m^{-1}; dash line: l=25μm, a=37,500m^{-1} (Xing *et al.*, 2011).

concentration, overpotential, and time according to Equations (25)–(28). These equations are solved by the time-dependent solver of COMSOL, and time stepping is from 0 to 2000s with an interval of 1s.

5.1 Transient of the coverage of intermediate species

Elemental step (19) happens on the surface of Pt site and thus results in the typical change of methanol ratio from zero to saturation. Figure 16 shows the influence of operating temperature, bulk methanol concentration, and applied overpotential on the transient of methanol coverage ratios (θ_M). As it clearly shows that methanol coverage ratios change from zero to saturation faster while higher operating temperature, methanol concentration, and overpotential are applied (see the solid lines). This is because methanol adsorption on Pt site, the first step of methanol oxidation (Equation (19)), could be accelerated by increasing temperature and methanol concentration. Furthermore, electro-oxidation of adsorbed methanol molecule, the second step of methanol oxidation (Equation (20)), is sensitive to overpotential. Higher overpotential could accelerate this step. The comparison of Figure 16a–c indicates that the operating temperature has a greater influence on θ_M compared to the other two parameters, methanol concentration and overpotential.

Adsorbed OH on Ru sites ($\theta_{OH,Ru}$), the intermediate species which are generated by hydrolysis of water on Ru active sites, approaches to saturation very fast under almost all operating temperature, methanol concentration, and overpotential. From Figure 17, we can see that $\theta_{OH,Ru}$ reach to saturation very shortly and the value of the saturation is very close to 1. This indicates that step (21.1) is not the rate-controlling step. The peaks in Figure 17 suggest the accumulation of $\theta_{OH,Ru}$ due to the faster generation rate according to Equation (21.2) and the slower consumption rate according to Equation (22). As same as Equation (20), Equation (21.2) is an electrochemistry step which related to electrical energy. The generation rate of $\theta_{OH,Ru}$ is highly dependent on overpotential. The operating overpotential and temperature have a greater influence on $\theta_{OH,Ru}$ compared to the methanol concentration. This is because methanol concentration affects Equations (19) and (20) significant, but it only has small influence on the accumulation and consumption of $\theta_{OH,Ru}$ according to Equation (22).

It is believed that the reaction of CO_{ads} to CO_2 occurs on Ru sites, and Pt sites serve as an active surface of adsorption and dehydrogenation of methanol (Gasteiger *et al.*, 1995, 2003; Kauranen and Skou, 1996; Kauranen *et al.*, 1996). As a result, it is reasonable of assuming that element step (20) occurred on Pt sites. CO_{ads} on Pt sites, which is the products of step (20), has great influence on the rate of step (22) because CO_{ads} is the reactants of step (22). The saturation value of CO_{ads} is very

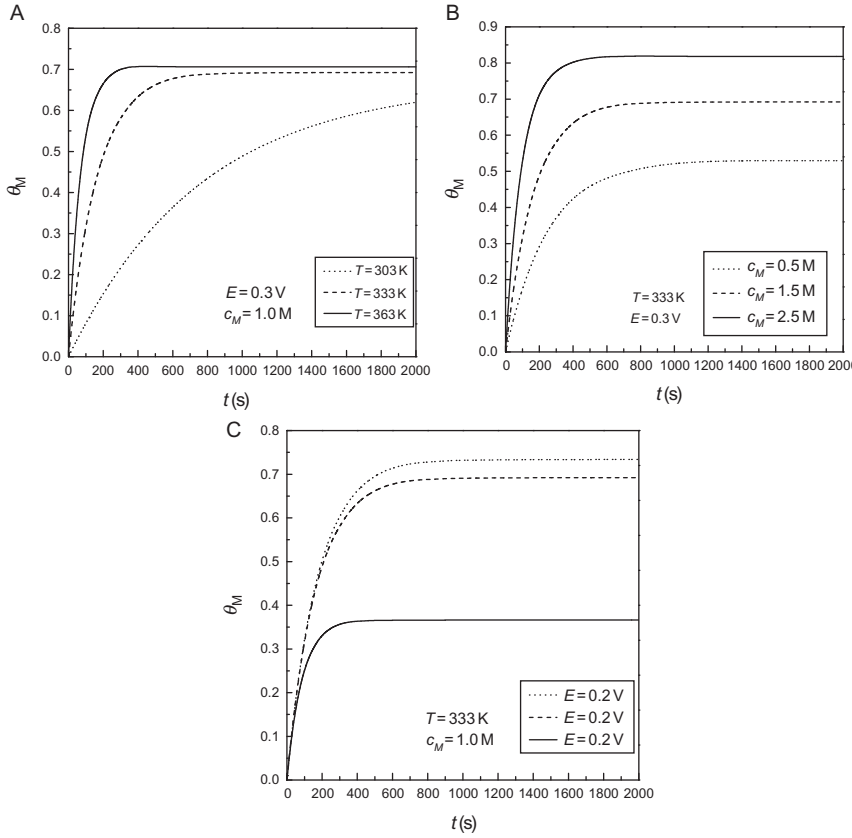

Figure 16 Transient of methanol coverage ratios with different operating (a) temperature, (b) methanol concentration, and (c) overpotential (Xing *et al.*, 2011).

small, says approximately five order of magnitude smaller than $OH_{ads,Ru}$, which is also the reactants of step (22). As we has discussed above, step (21.1) is impossible to become the rate-controlling step due to the extreme fast reaction rate. We can conclude that the rate of the whole methanol oxidation process is controlled by steps (19), (20), or (22) in which reactants CO_{ads} and $OH_{ads,Ru}$ are involved. The operating temperature has a greater influence on $\theta_{CO,Pt}$ compared to the other two parameters, overpotential and methanol concentration.

5.2 Transient of the current density

Figure 18 shows the transient variation in current density at different operating conditions. Typically, the steady state is approached within 2000–4000 s. The time for the transient current density to approach a steady

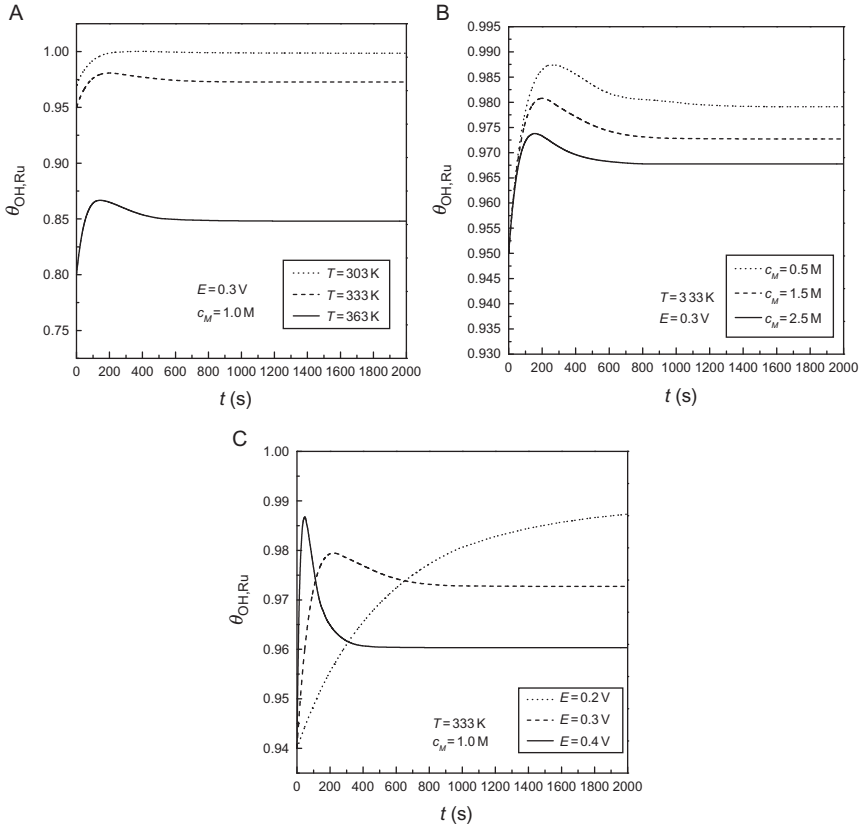

Figure 17 Transient of coverage ratios of adsorbed OH on Ru sites with different operating (a) temperature, (b) methanol concentration, and (c) overpotential.

state decreased when temperature, methanol concentration, and overpotential increased. The operating temperature affects the current density more than the methanol concentration and overpotential. The influence on i_T is similar to its influence on θ_M. Moreover, the curves of i_T and $\theta_{CO,Pt}$ have great similarities in respect of the shape and the time variation, although $\theta_{CO,Pt}$ is some four to eight orders of magnitude smaller than θ_M. This is because elemental step (21.1), which happens on the surface of Ru site, is extremely fast and resulted in the very fast and high saturation (very close to 1) of $\theta_{OH,Ru}$ on the surface of Ru site (Sun *et al.*, 2010).

As stated in Equation (30), current density is a function of the product of $\theta_{CO,Pt}$ and $\theta_{OH,Ru}$. The current density would have no relationship to $\theta_{OH,Ru}$ if $\theta_{OH,Ru}$ could be considered as constant (the value is 1). We may reasonably conclude that step (21.1) is not the rate-determining step; thus, the whole rate of the electrochemical reaction is determined by step (20).

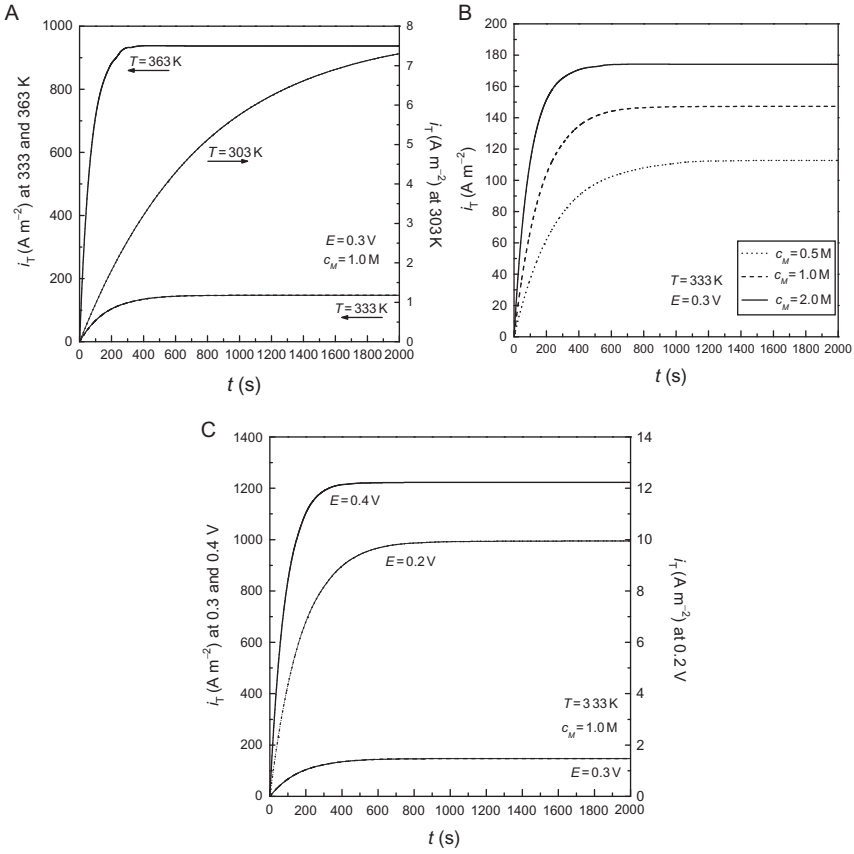

Figure 18 Transient of current density with different operating (a) temperature, (b) methanol concentration, and (c) overpotential (Xing *et al.*, 2011).

In addition, step (19) might be the rate-determining step because it provides the reactant to step (20).

6. CONCLUSIONS

DMFCs have reached a high level of development and are now set to function as power sources for a range of mobile applications. This position has largely been brought about by the convenience of storage of the liquid fuel. It is true however to say that the power performance of the DMFC does not match that of the sister fuel cell using hydrogen as fuel. Even with an order of magnitude greater catalyst loading (compare to hydrogen PEMFC), the power performance of the DMFC is at best half that of the PEMFC. This makes it unlikely that the DMFC will see applications in transportation except perhaps in niche area. The DMFC responds quite

rapidly to changes in operating conditions and is a suitable power source for portable applications where variations in operating conditions arise.

LIST OF SYMBOLS

LATIN LETTERS

a	specific electrode area, m^{-1}
C	dimensionless concentration
c	Concentration, $\mathrm{mol\,m}^{-3}$
D_0	diffusion coefficient, $\mathrm{m}^2\mathrm{s}^{-1}$
D_e	effective diffusion coefficient, $\mathrm{m}^2\mathrm{s}^{-1}$
E	overpotential, V
F	Faraday constant, $\mathrm{C\,mol}^{-1}$
I	dimensionless current density
I_al	dimensionless adsorption limiting current density
i	current density, $\mathrm{A\,m}^{-2}$
i_0	exchange current density, $\mathrm{A\,m}^{-2}$
i_al	adsorption limiting current density, $\mathrm{A\,m}^{-2}$
i_crit	critical current density, $\mathrm{A\,m}^{-2}$
k_4	surface rate constant, $\mathrm{mol\,m}^{-2}\mathrm{s}^{-1}$
l	thickness of porous anode, m
N_M	flux of methanol, $\mathrm{mol\,m}^{-2}\mathrm{s}^{-1}$
n	number of electrons involved in reaction
R_g	universal gas constant, $\mathrm{J\,mol}^{-1}\mathrm{K}^{-1}$
R	apparent reaction rate, $\mathrm{mol\,m}^{-2}\mathrm{s}^{-1}$
r_4	surface reaction rate, $\mathrm{mol\,m}^{-2}\mathrm{s}^{-1}$
s	dimensionless modulus$=ai_0l^2/(nFD_\mathrm{e}c_\mathrm{M}^0)$
T	temperature, K
t	time, s
X	dimensionless distance
x	distance, m

GREEK LETTERS

α	charge transfer coefficient
β	parameters$=(1-\beta_3)F/RT=(1-\beta_4)F/RT$, V^{-1}
ε	porosity
ϕ^0	potential of open circuit, V
ϕ^1	potential of electrolyte, V
ϕ^m	potential of matrix, V

κ_e	effective conductivity, $\Omega^{-1}m^{-1}$
$(_{\downarrow}(H_{\downarrow}2O)$	empirical model coefficients
μ	dimensionless modulus$=ai_0l^2/(nFD_ec^0M)$
ν^2	dimensionless parameter$=ai_0l^2\beta/\kappa_e$
θ	coverage ratio
ξ	effectiveness
Ψ	dimensionless relative overpotential$=\Phi/\beta E^0$

SUBSCRIPTS AND SUPERSCRIPTS

0	at the boundary of the diffusion layer $X=1$
a	anode
ads	adsorbed
c	cathode
CO	absorbed carboxide
conc	concentration
e	effective
i	species i
loc	local state
M	methanol
OH	absorbed hydroxide
Pt	platinum
ref	reference
Ru	ruthenium
T	total or apparent state

ACKNOWLEDGMENTS

The authors gratefully acknowledge the financial support from EPSRC Supergen Fuel Cell Consortium award.

REFERENCES

Argyropoulos, P., Scott, K. and Taama, W. M., *J. Power Sour.* **79,** 169 (1999a).
Argyropoulos, P., Scott, K. and Taama, W. M., *J. Power Sour.* **79,** 184 (1999b).
Argyropoulos, P., Scott, K. and Taama, W. M., *J. Power Sour.* **87,** 153 (2000).
Argyropoulos, P., Scott, K. and Taama, W. M., *J. Appl. Electrochem.* **31,** 13 (2001).
Argyropoulos, P., Scott, K., Shukla, A. K. and Jackson, C., *J. Power Sour.* **123,** 190 (2003).
Aricò, A. S., Kim, H., Antonucci, V., Shukla, A. K., Ravikumar, M. K. and Giordano, N., *Electrochim. Acta* **39,** 691 (1994a).
Aricò, A. S., Antonucci, V., Giordano, N., Shukla, A. K., Ravikumar, M. K., Roy, A., Barman, S. R. and Sarma, D. D., *J. Power Sour.* **50,** 295 (1994b).
Bagotzky, V. S. and Vassilyer, Yu.B., *Electrochim. Acta* **12,** 1323 (1967).
Baldauf, M. and Preidel, W., *J. Power Sour.* **84,** 161 (1999).

Basri, S., Kamarudin, S. K., Daud, W. R. W., Yaakub, Z., Ahmad, M. M., Hashim, N. and Hasran, U. A., *Int. J. Hydrogen Energy* **34,** 5759 (2009).
Baxter, S. F., Battaglia, V. S. and White, R. E., *J. Electrochem. Soc.* **146,** 437 (2000).
Bernardi, D. M. and Verbrugge, M. W., *J. Electrochem. Soc.* **139,** 2477 (1992).
Buttin, D., Dupont, M., Straumann, M., Gille, R., Dubois, J.-C., Ornelas, R., Fleba, G. P., Ramuni, E., Antonucci, V., Arico, A. S., Creti, P., Modica, E., Pham-Thi, M. and Ganne, J.-P., *J. Appl. Electrochem.* **31,** 275 (2001).
Cai, W. W., Li, S. T., Feng, L. G., Zhang, J., Song, D. T., Xing, W. and Liu, C. P., *J. Power Sour.* **196,** 3781 (2011).
Chan, L., Allen, R. G. and Scott, K., *J. Power Sour.* **161,** 11 (2006).
Chippar, P., Ko, J. and Ju, H., *Energy* **35,** 2301 (2010).
Cruickshank, J. and Scott, K., *J. Power Sour.* **70,** 40 (1998).
Dargahi, M. and Rezanezhad, M., *Mod. Appl. Sci.* **3,** 45 (2009).
Divisek, J., Fuhrmann, J., Gartner, K. and Jung, R., *J. Electrochem. Soc.* **150,** A811 (2003).
Dohle, H. and Wippermann, K., *J. Power Sour.* **135,** 152 (2004).
Dohle, H., Divisek, J. and Jung, R., *J. Power Sour.* **86,** 469 (2000).
Freelink, T., Visschev, W. and van Veen, J. A. R., *Langmuir* **12,** 3702 (1996).
García, B. and Weidner, J., *in* ''Modern Aspects of Electrochemistry'' (R. E. White, Ed.), pp. 229–284. Springer, New York. No. 40 (2007).
García, B., Sethuraman, V., Weidner, J., White, E. R. and Dougal, R., *J. Fuel Cell Sci. Technol.* **1,** 43 (2004).
Gasteiger, H. A., Markovic, N., Ross, P. N., Jr. and Cairns, E. J., *J. Electrochem. Soc.* **141,** 1795 (1995).
Gasteiger, H. A., Markovic, N., Ross, P. N., Jr. and Cairns, E. J., *J. Phys. Chem.* **97,** 12020 (2003).
Gerteisen, D., *J. Power Sour.* **195,** 6719 (2011).
Gottesfeld, S., *J. Power Sour.* **171,** 37 (2007).
Gottesfeld, S., Ren, X., Zelenay, P., Dinh, H., Guyon, F. and Davey, J., *in* Proceedings of the Fuel Cell Seminar, Portland, Oregon, USA, 30th October–2nd November, Advances in Direct Methanol Fuel Cell Science & Technology at Los Alamos National Laboratory (2000).
Guarnieri, M., Noto, V. D. and Moro, F., *IEEE Trans. Ind. Electron.* **57,** 1865 (2010).
Gurau, B. and Smotkin, E. S., *J. Power Sour.* **112,** 339 (2002).
Gurau, V., Liu, H. and Kakac, S., *AIChE J.* **44,** 2410 (1998).
He, Y. L., Li, X. L., Miao, Z. and Liu, Y. W., *Appl. Ther. Eng.* **29,** 1998 (2009).
Heinzel, A. and Barragán, V. M., *J. Power Sour.* **84,** 70 (1999).
Jung, D. H., Lee, C. H., Kim, C. S. and Shin, D. R., *J. Power Sour.* **71,** 169 (1998).
Kauranen, P. S. and Skou, E., *J. Electroanal. Chem.* **408,** 189 (1996).
Kauranen, P. S., Skou, E. and Munk, J., *J. Electroanal. Chem.* **404,** 1 (1996).
Ko, D. H., Lee, M. J., Jang, W. H. and Krewer, U., *J. Power Sour.* **180,** 71 (2008).
Kordesch, K. and Simader, G., ''Fuel Cells and Their Applications''. VCH, Weinheim (1994).
Krewer, U., Song, Y., Sundmacher, K., John, V., Lubke, R., Matthies, G. and Tobiska, L., *Chem. Eng. Sci.* **59,** 119 (2004).
Krewer, U., Christov, M., Vidakovic, T. and Sundmacher, K., *J. Electroanal. Chem.* **589,** 148 (2006).
Kulikovsky, A. A., *J. Appl. Electrochem.* **30,** 1005 (2000).
Kulikovsky, A. A., *Electrochem. Commun.* **4,** 939 (2002).
Kulikovsky, A. A., *Electrochem. Commun.* **5,** 530 (2003a).
Kulikovsky, A. A., *Electrochem. Commun.* **5,** 1030 (2003b).
Ley, K. L., Liu, R., Pu, C., Fan, Q., Leyarovska, N., Serge, C. and Smotkin, E. S., *J. Electrochem. Soc.* **144,** 1543 (1997).
Liu, W. and Wang, C. Y., *J. Electrochem. Soc.* **154,** B352 (2007a).

Liu, W. and Wang, C. Y., *J. Power Sour.* **164,** 189 (2007b).
Lizcano-Valbuena, W. H., Paganin, V. A. and Gonzalez, E. R., *Electrochim. Acta* **47,** 3715 (2002).
Meyers, J. P. and Newman, J., *J. Electrochem. Soc.* **149,** A710 (2002a).
Meyers, J. P. and Newman, J., *J. Electrochem. Soc.* **149,** A718 (2002b).
Meyers, J. P. and Newman, J., *J. Electrochem. Soc.* **149,** A729 (2002c).
Munichandraiah, N., McGrath, K., Prakash, G. K. S., Aniszfeld, R. and Olah, G. A., *J. Power Sour.* **117,** 98 (2003).
Murgia, G., Pisani, L., Shukla, A. K. and Scott, K., *J. Electrochem. Soc.* **150,** A1231 (2003).
Narayanan, S. R., Kindler, A., Jeffries-Nakamura, B., Chun, W., Frank, H., Smart, M., Surampudi, S. and Halpert, G., *in* ''Proton Conducting Membrane Fuel Cells I'' (S. Gottesfeld, G. Halpert and A. Landgrebe, Eds.), The Electrochemical Society Inc., Pennington, NJ(1995) PV 95-23, 261.
Newman, J., ''Electrochemical Systems''. 3rd ed. Prentice-Hall, New Jersey (2004).
Newman, J. and Tobias, C., *J. Electrochem. Soc.* **109,** 1183 (1962).
Nordlund, J. and Lindbergh, G., *in* ''Direct Methanol Fuel Cells'' (S. R. Narayanan, S. Gottesfeld and T. Zawodzinski, Eds.), The Electrochemical Society Inc., Pennington, NJ(2001) PV 2001-4, 331.
Nordlund, J. and Lindbergh, G., *J. Electrochem. Soc.* **149,** A1107 (2002).
Nordlund, J. and Lindbergh, G., *J. Electrochem. Soc.* **151**(9), A1357 (2004).
Oliveira, V. B., Falcão, D. S., Rangel, C. M. and Pinto, A. M. F. R., *Int. J. Hydrogen Energy* **32,** 415 (2007).
Ravikumar, M. K. and Shukla, A. K., *J. Electrochem. Soc.* **143,** 2601 (1996).
Ren, X., Henderson, W. and Gottesfeld, S., *J. Electrochem. Soc.* **144,** L267 (1997).
Ren, X., Springer, T. E., Zawodzinski, T. A. and Gottesfeld, S., *J. Electrochem. Soc.* **147,** 466 (2000a).
Ren, X., Zelenay, P., Thomas, S., Davey, J. and Gottesfeld, S., *J. Power Sour.* **86,** 111 (2000b).
Schultz, T., Zhou, S. and Sundmacher, K., *Chem. Eng. Technol.* **24,** 1223 (2001).
Scott, K., *in* ''Handbook of Fuel Cell: Fundamentals Technology and Applications'' (W. Vielstich, A. Lamm and H. A. Gasteiger, Eds., Vol. 4, J. Wiley and Sons, England (Chapter 64) (2003).
Scott, K. and Argyropoulos, P., *J. Elctroanal. Chem.* **567,** 103 (2004a).
Scott, K. and Argyropoulos, P., *J. Power Sour.* **137,** 228 (2004b).
Scott, K. and Shukla, A., *in* ''Modern Aspects of Electrochemistry'' (R. E. White, Ed.), Springer, New York No. 40, p. 127, (2007).
Scott, K. and Sun, Y. P., *in* ''Modern Aspects of Electrochemistry'' (C. Vayenas and M. Gamboa-Adelco, Eds.), Springer, New York, No. 41, p. 221 (2007).
Scott, K., Taama, W. and Cruickshank, J., *J. Power Sour.* **65,** 159 (1997).
Scott, K., Taama, W. M., Kramer, S., Argyropoulos, P. and Sundmacher, K., *Electrochim. Acta* **45,** 945 (1999a).
Scott, K., Argyropoulos, P. and Sundmacher, K., *J. Electroanal. Chem.* **477,** 97 (1999b).
Scott, K., Argyropoulos, P. and Taama, W. M., *Trans. IChemE* **78,** 881 (2000).
Scott, K., Argyropoulos, P., Yiannopoulos, P. and Taama, W. M., *J. Appl. Electrochem.* **31,** 823 (2001).
Shao, Z. G., Lin, W. F., Zhu, F. Y., Christensen, P. A., Li, M. Q. and Zhang, H. M., *J. Electrochem. Commun.* **8,** 5 (2006).
Shivhare, M., Allen, R., Scott, K., Morris, A. and Martin, E., *J. Electroanal. Chem.* **595,** 145 (2006).
Shivhare, M., Jackson, C., Scott, K. and Martin, E., *J. Power Sour.* **173,** 240 (2007).
Shukla, A. K., Ravikumar, M. K., Neergat, M. and Gandhi, K. S., *J. Appl. Electrochem.* **29,** 129 (1999).

Shukla, A. K., Jackson, C. L., Scott, K. and Raman, R. K., *Electrochim. Acta* **47,** 3401 (2002a).
Shukla, A. K., Jackson, C. L., Scott, K. and Murgia, G., *J. Power Sour.* **111,** 43 (2002b).
Simoglou, A., Argyropoulos, P., Martin, E. B., Scott, K., Morris, A. J. and Taama, W. M., *Chem. Eng. Sci.* **56,** 6761 (2001a).
Simoglou, A., Argyropoulos, P., Martin, E. B., Scott, K., Morris, A. J. and Taama, W. M., *Chem. Eng. Sci.* **56,** 6773 (2001b).
Springer, T. E., Zawodzinski, T. A. and Gottesfeld, S., *J. Electrochem. Soc.* **138,** 2334 (1991).
Stanley, K. G., Wu, Q. M. J., Vanderhoek, T. and Nikumb, I., *in* ''IEEE CCEC 2002: Canadian Conference on Electrical and Computer Engineering, 12nd to 15th May'' (W. Kinsner, A. Sebak and K. Ferens, Eds., Vol. 1–3, (2002).
Sun, Y. P., *J. Chem. Ind. Eng.* **58**(9), 2161(2007) (in Chinese).
Sun, Y. P. and Scott, K., *Fuel Cell* **4**(1/2), 30 (2004a).
Sun, Y. P. and Scott, K., *Chem. Eng. J.* **1024**(1), 83 (2004b).
Sun, Y. P. and Xing, L., *CIESC* **60**(1), 55 (in Chinese), (2009).
Sun, Y. P., Xing, L. and Scott, K., *J. Power Sour.* **195,** 1 (2010).
Sundmacher, K. and Scott, K., *Chem. Eng. Sci.* **54,** 2927 (1999).
Sundmacher, K., Schultz, T., Zhou, S., Scott, K., Ginkel, M. and Gilles, E. D., *Chem. Eng. Sci.* **56,** 333 (2001).
Surampudi, S., Narayanan, S. R., Vamos, E., Frank, H., Halpert, G., LaConti, A., Kosek, J., Surya Prakash, G. K. and Olah, G. A., *J. Power Sour.* **47,** 377 (1994).
Um, S., Wang, C. Y. and Chen, K. S., *J. Electrochem. Soc.* **147,** 4485 (2000).
Valdez, T. I., Narayanan, S. R., Frank, H. and Chun, W., *in* Proceedings of the 12th Annual battery Conference on Applications and Advances, Long Beach, 14th–17th January, (1997a).
Valdez, T. I., Narayanan, S. R., Frank, H. and Chun, W., *in* ''Annual Battery Conference on Application and Advances''. Long Beach, USA (1997b).
Verbrugge, M. W., *J. Electrochem. Soc.* **136,** 417 (1989).
Wang, C. Y., *Chem. Rev.* **104,** 4727 (2004).
Wang, Z. H. and Wang, C. Y., *in* ''Direct Methanol Fuel Cells'' (S. R. Narayanan, S. Gottesfeld and T. Zawodzinski, Eds.), The Electrochemical Society Inc., Pennington, NJ PV 2001-4, p. 286, (2001).
Wang, M. H., Guo, H. and Ma, C. F., *J. Fuel Cell Sci. Technol.* **3,** 202 (2006).
Xing, L., Scott, K. and Sun, Y. P. *Int. J. Electrochem.* **2011**, 14 (2011).
Xu, C. and Faghri, A., *J. Power Sour.* **195,** 7011 (2010).
Zenith, F. and Krewer, U., *J. Process Control* **20,** 630 (2010).
Zou, J. Q., He, Y. L., Miao, Z. and Li, X. Y., *Int. J. Hydrogen Energy* **35,** 7206 (2010).